ChemPubSoc Europe

DOI: 10.1002/chem.201701059

CHEMISTRY A European Journal Full Paper

Catalysis |*Hot Paper*|

Interplay of Electronic Cooperativity and Exchange Coupling in Regulating the Reactivity of Diiron(IV)-oxo Complexes towards C–H and O–H Bond Activation

Azaj Ansari[+],[b] Mursaleem Ansari[+],[c] Asmita Singha,[d] and Gopalan Rajaraman*[a]

Abstract: Activation of inert C–H bonds such as those of methane are extremely challenging for chemists but in nature, the soluble methane monooxygenase (sMMO) enzyme readily oxidizes methane to methanol by using a diiron(IV) species. This has prompted chemists to look for similar model systems. Recently, a (μ-oxo)bis(μ-carboxamido)diiron(IV) ($[Fe^{IV}_2O(L)_2]^{2+}$ L = *N*,*N*-bis-(3′,5′-dimethyl-4′-methoxypyridyl-2′-methyl)-*N*′-acetyl-1,2-diaminoethane) complex has been generated by bulk electrolysis and this species activates inert C–H bonds almost 1000 times faster than mononuclear Fe^{IV}=O species and at the same time selectively activates O–H bonds of alcohols. The very high reactivity and selectivity of this species is puzzling and herein we use extensive DFT calculations to shed light on this aspect. We have studied the electronic and spectral features of diiron $\{Fe^{III}$-μ(O)-$Fe^{III}\}^{+2}$ (complex **I**), $\{Fe^{III}$-μ(O)-$Fe^{IV}\}^{+3}$ (**II**), and $\{Fe^{IV}$-μ(O)-$Fe^{IV}\}^{+4}$ (**III**) complexes. Strong antiferromagnetic coupling between the Fe centers leads to spin-coupled $S=0$, $S=3/2$, and $S=0$ ground state for species **I**–**III** respectively. The mechanistic study of the C–H and O–H bond activation reveals a multistate reactivity scenario where C–H bond activation is found to occur through the $S=4$ spin-coupled state corresponding to the high-spin state of individual Fe^{IV} centers. The O–H bond activation on the other hand, occurs through the $S=2$ spin-coupled state corresponding to an intermediate state of individual Fe^{IV} centers. Molecular orbital analysis reveals σ–π/π–π channels for the reactivity. The nature of the magnetic exchange interaction is found to be switched during the course of the reaction and this offers lower energy pathways. Significant electronic cooperativity between two metal centers during the course of the reaction has been witnessed and this uncovers the reason behind the efficiency and selectivity observed. The catalyst is found to prudently choose the desired spin states based on the nature of the substrate to effect the catalytic transformations. These findings suggest that the presence of such factors play a role in the reactivity of dinuclear metalloenzymes such as sMMO.

Introduction

The C–H bond activation of alkanes have been studied immensely over the last decade as it offers a direct way to introduce functional groups into a relatively inert hydrocarbon in a cost-effective manner and this process has high industrial application.[1] High-valent metal-oxo complexes have a versatile role in C–H bond activation, and this is evident from a variety of biological transformations such as hydroxylation, epoxidation, dehydrogenation, halogenations, etc. performed by these species.[2] Enzymes activating O_2 generally employ a transition metal such as Fe, Mn, Co, or Cu where the oxidation state of the metal ion can also be fine-tuned.[3] The catalytic pathway includes oxygen activation followed by the formation of highly reactive intermediates such as oxo, peroxo, hydroperoxo, and superoxo species.[3a–e,4] In the last decade, a large number of model complexes have been synthesized to understand the mechanism of C–H bond activation, which mimics the catalytic activity of enzymes.[3a–e,5]

Several high-valent iron-oxo intermediates are also reported to perform stereo- and regioselective hydroxylation and epoxidation of organic substrates.[4a,b,6] The oxoiron(IV) unit remains the center of investigation as it is involved in many catalytic cycles of non-heme iron enzymes, and analogous biomimetic oxidants can perform hydroxylation and O atom transfer reactions.[3a–e,4a,b,6b,7] Numerous efforts have been made to understand the mechanism of C–H bond activation occurring in cytochrome P450 enzymes, possessing one of the well-character-

[a] *Prof. G. Rajaraman*
Department of Chemistry, Indian Institute of Technology Bombay
Powai, Mumbai, Maharashtra, 400076 (India)
E-mail: rajaraman@chem.iitb.ac.in

[b] *Dr. A. Ansari*[+]
Department of Chemistry, CUH Haryana, Haryana 123031 (India)

[c] *M. Ansari*[+]
Department of Chemistry, IIT Bombay, Mumbai, 400076 (India)

[d] *A. Singha*
Department of Chemistry, IIT Bombay, Mumbai, 400076 (India)

[+] *These authors contributed equally to this work.*

Supporting information and the ORCID identification number for the author of this article can be found under https://doi.org/10.1002/chem.201701059: Tables with selected structural parameters of optimized geometries, spin densities, orbital overlap, electronic configurations, Mossbauer parameters, solvent and gap phase energies, relative energies computed by using B3LYP and OPBE functionals, entropic contributions to various species computed, coordinates of all the species. In addition, computed NBO plots, additional spin density plots of other spin states, absorption spectra computed for other species are given.

ized oxoiron(IV) radical cation units in its active site.[1b,e,8] The mechanistic pathways adapted by the enzymes and the mimics are generally common and this offers a way to improve the efficiency and selectivity of bio-mimic catalysts.[1b,e,3b,9]

In addition, mononuclear metal-oxo species, oxygen bridged iron, copper and manganese {M-μ(O)-M} dimer species are also found to play an important role in biological systems, as evident from the presence of these dinuclear species at the active site of numerous enzymes like tyrosenase, catechol oxidase, methane monooxygenase, arginase, etc.[2b,10] These enzymes utilize dinuclear metal centers in catalyzing various biological transformations.[1d,2a,b,11] During the last few years, several models containing dimeric μ-oxo bridged metal ions coordinated with various types of ligands have been investigated. Among the dinuclear species, high-valent diiron oxo complexes have gained considerable attention as they are found to be the active species of most of the hydroxylating and O_2-dependent dehydrogenating enzymes such as methane monooxygenase, toluene monooxygenase, fatty acid desaturases, etc.[1d,2a,b,12]

There are two types of methane monooxygenase enzyme (MMO), one being membrane bound particulate MMO (pMMO) and the other being cytoplasmic soluble MMO (sMMO). Although particulate MMO utilizes a multicopper center,[13] sMMO possesses a diiron unit in its active form.[14] Several model complexes have been reported based on the diamond core of sMMO, which is comprised of an antiferromagnetically coupled $\{Fe_2(\mu\text{-}O)_2\}$ unit, to understand the action of sMMO on methane.[2b,9d,14a,b,15]

Among several model systems reported, the (μ-oxo)bis(μ-carboxamido)diiron(III) complex has gained attention as its oxidized form exhibits very high reactivity towards strong C–H bonds.[14a] Upon oxidation of (μ-oxo)bis(μ-carboxamido)diiron(III) by performing cyclic voltammetry experiments, the (μ-oxo)bis(μ-carboxamido)Fe^{IV} dimer is formed in 70% yield (Scheme 1).[14b,16] This species has been found to oxidize inert C–H bonds such as those in cyclohexane as well as stronger O–H bonds such as those in aliphatic alcohols while keeping the relatively weaker C–H bonds intact. Although these species have been characterized by X-ray absorption spectroscopy and other techniques, the origin of such high reactivity and selectivity is still unknown.[14b]

Theoretical studies play an important role in this area to obtain insight into the electronic structure of the catalytically active species, and also to probe the mechanism of the catalytic transformations.[9d,17] In the literature, there are numerous reports on the electronic structure and mechanistic studies of mononuclear high-valent iron-oxo species but there are only limited studies on the dinuclear iron-oxo species.[8f,17c,18] This is essentially owing to the presence of numerous spin states arising from the exchange coupling between the two metal centers, and these states are often challenging to compute.[19] In this work, we aim to discuss the electronic structure of the dinuclear iron oxidants to uncover the high reactivity observed for the μ-oxo bis(μ-carboxamido) diiron(IV) complex towards activating O–H and C–H bonds by using density functional theory. Particularly, we aim to answer the following intriguing questions: 1) how does the electronic structure of μ-oxo diiron

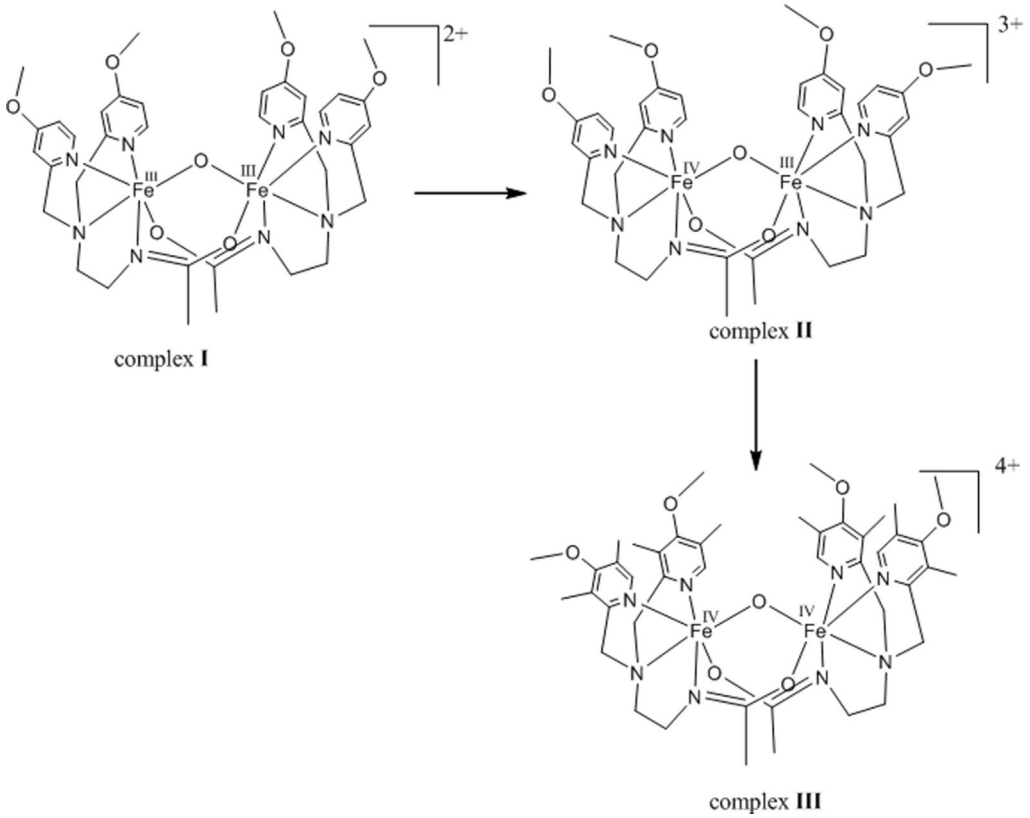

Scheme 1. Schematic diagram illustrating various species involved in the formation of the μ-oxo high-valent diiron(IV) catalyst.

species evolve as the oxidation state increases from III to IV? 2) how does the complex spin state pattern have an effect on the observed spectral parameters (absorption, Mössbauer, and EPR)? 3) what are the mechanistic pathways by which the diiron(IV)-oxo activates the C–H and O–H bonds? 4) what is the origin of the high selectivity and efficiency observed for this species?

Computational Details

All calculations were performed by using the Gaussian 09 suite of programs.[20] In our earlier theoretical studies on high-valent metal-oxo species, we have employed a bunch of functionals (such as B3LYP, B3LYP-D2, wB97XD, B97D, M06-2X, OLYP, TPPSh, and MP2) among which B3LYP, B3LYP-D2, and wB97XD were found to predict the correct spin state structures.[21] Among the three tested functionals, the B3LYP functional incorporating dispersion correction as proposed by Grimme et al. was found to be superior.[21–22] On the dinuclear front, a detailed method assessment performed on μ-nitrido-diiron(IV)-oxo species by using the B3LYP, B3LYP*, BP86, M06-L, and PBE0 functionals reveals that the B3LYP functional is able to reproduce the structure, spin state patterns, and spectral parameters. To further validate the spin state energetics for complexes **I** to **III**, here we have performed calculations by using OPBE and B3LYP functionals incorporating the dispersion effects proposed by Grimme et al.[22b] Both the functionals predict the same ground states for all the species computed and also yield very similar splitting patterns (see Table S10 in the Supporting Information). By analyzing these results along with all the previous observations, here we have chosen the B3LYP-D3 functional for our study. The LACVP basis set comprising the LanL2DZ—Los Alamos effective core potential for Fe[23] and a 6-31G[24] basis set for the other atoms (carbon, nitrogen, oxygen, and hydrogen) (B-I) were employed for the geometry optimization and frequency calculations. Single point calculations were performed by using a def2-TZVP[25] basis set (B-II) on the optimized geometries. The solvation energies were computed by using the polarizable continuum model (PCM) solvation model where acetonitrile has been used as the solvent. It has been reported that the spin state energies of mono and dinuclear Fe^{IV}=O species are strongly influenced by solvation energies.[26] To ascertain this effect in our calculations, we have also computed the relative energies of all species in the gas phase. Comparison between these two sets are given in the Supporting Information (Table S9) and from this table, it is clear that the solvation significantly influences the spin state gaps. However, the ground state as well as the trends are predicted to be very similar between these two sets. As solvation-incorporated energies are more appropriate for our complexes, only these energies will be discussed further. The fragment approach available in the Gaussian 09 program has been employed to obtain open-shell singlet states and also to converge difficult multiplets. All reported energies are B3LYP-D3 solvation energies (at B-II level) incorporating free energy corrections (at B-I level) at 298.15 K. Although inclusion of solvent in the optimization was found to influence the spin state energies to a certain extent,[27] the trend for the computed energetics are similar as shown earlier[28] and therefore here we have performed only a single point calculation including solvation using the PCM model. Additionally, for comparison, we have also given zero-point energy (ZPE) corrected values in the Supporting Information (see Figure S9 for C–H activation and Figure S10 for O–H activation). The transition states were characterized by a single imaginary frequency, which pertains to the desired motion as visualized in Chemcraft[29] and Molden.[30] In the diiron complexes, the magnetic exchange (*J*) between both iron centers is computed by employing the following spin Hamiltonian [Eq. (1)]:

$$\mathscr{H} = -JS_1 \cdot S_2 \qquad (1)$$

In the above equation, the positive *J* value corresponds to a ferromagnetic interaction whereas a negative *J* value corresponds to an antiferromagnetic interaction. To compute *J* values, the energy of the high-spin state (E_{HS}) and the low-spin state (E_{BS}) are calculated by using the broken symmetry (BS) approach developed by Noodleman.[31] All spectroscopic parameters are calculated by using the ORCA 2.8 software[32] incorporating relativistic effects by the zeroth-order regular approximation method (ZORA)[33] involving the COSMO solvation method. The MB-Isomer shifts (IS) were computed based on the calibration constants reported by Römelt et al. and 0.16 barn was used for the calculation of the quadrupole moment of ^{57}Fe nuclei by using the TZVP basis set.[34] Time-dependent density functional theory (TD-DFT) implemented in the ORCA program was employed for the calculation of excitation energies. Molecular orbital (MO) and natural bond order (NBO) analyses[35] were performed by using Gaussian 09 and visualizations were examined by using Chemcraft software. A common notation of $^{mult}\mathbf{A}_{O/C\text{-}H\ spin\text{-}state}$ has been used throughout, where the superscript mult denotes the total multiplicity; A indicates the complex number and spin state in the subscript denotes the different spin configurations (high-spin, low-spin, etc.) of the Fe atoms. The O–H/C–H characters in the subscript indicate the transition state corresponding to the O–H/C–H bond activation.

Results

The starting point for this study is the dinuclear Fe^{III}-μ(O)-Fe^{III} moiety $[Fe^{III}_2O(L)_2]^{2+}$ (complex **I**, where L = *N*,*N*-bis-(3′,5′-dimethyl-4′-methoxypyridyl-2′-methyl)-*N*′-acetyl-1,2-diaminoethane).[14b] Earlier experimental studies suggest that electrolysis of complex **I** at potentials above +0.70 V leads to the formation of complex **II**. Increasing the bulk electrolysis potential to +1.70 V after the formation of complex **II** leads to the formation of complex **III** as shown in Scheme 1.[14b] We will begin our discussion with species **I**–**III**, examining the structures and spin state energetics in detail before we move to probe the reactivity aspects of complex **III**. The Fe^{III} center in the complex **I** can be high-spin (hs; $S = 5/2$) or intermediate-spin (is; $S = 3/2$) or low-spin (ls; $S = 1/2$). Similarly, the Fe^{IV} centers in complexes **II** and **III** can possess hs ($S = 2$), is ($S = 1$), or ls ($S = 0$) states. These two centers are coupled through the μ-oxo and two carboxamido bridges, leading to ferro/antiferromagnetically coupled spin states characterized by the total spin quantum number *S*. As the ligand environment is the same for both the metal centers, one can assume that both the metal centers are likely to exhibit the same type of spin states (that is, hs on both Fe^{III}). Based on these criteria, we have restricted our calculations to the same type of spin states on both the metal centers for complexes **I** and **III**, whereas for complex **II** other combinations have also been computed.

Electronic structures and energetic of complexes I–III

Complex I {Fe^{III}-μ(O)-Fe^{III}}

There are six different spin states: $^{11}\mathbf{I}_{hs}$, $^{1}\mathbf{I}_{hs}$, $^{7}\mathbf{I}_{is}$, $^{1}\mathbf{I}_{is}$, $^{3}\mathbf{I}_{ls}$, and $^{1}\mathbf{I}_{ls}$ are possible for this species and the explicit electronic configurations for each of the Fe atoms are given in Table 1. Here, the $^{1}\mathbf{I}_{hs}$ singlet state is found to be the ground state, suggesting antiferromagnetic coupling between the Fe^{III} centers. This is followed by the $^{11}\mathbf{I}_{hs}$, $^{7}\mathbf{I}_{is}$, $^{1}\mathbf{I}_{is}$, $^{3}\mathbf{I}_{ls}$, and $^{1}\mathbf{I}_{ls}$ states with energy margins of 25.0, 101.9, 101.2, 125.2, and 178.6 kJ mol^{-1}, respectively. The energetics reveal that the Fe^{III} centers possessing an intermediate spin state are also coupled antiferromagnetically whereas the Fe^{III} centers possessing low-spin configurations are found to be coupled in a ferromagnetic fashion. This difference in coupling is attributed to the nature of the orbital overlap between the two magnetic centers. As both high-spin and intermediate-spin Fe^{III} centers possess unpaired electrons in the e_g orbital, this results in an efficient overlap and hence antiferromagnetic interaction. For the low-spin Fe^{III} centers (t_{2g}^5 configuration), the unpaired electron is found to reside in the d_{xy} orbital and these orbitals are orthogonal between the two Fe^{III} centers, yielding a ferromagnetic coupling. The computed data is consistent with the experimental observation of an antiferromagnetic coupling between the two high-spin Fe^{III} centers, resulting in an $S=0$ ground state.[14] This result is also consistent with other dinuclear {Fe^{III}-μ(O)-Fe^{III}} moieties where $S=0$ is generally found to be the ground state. The optimized structure and the spin density plot of the $^{1}\mathbf{I}_{hs}$ state are shown in Figure 1a and b where both the Fe centers are in a distorted octahedral geometry. Selected structural parameters and spin densities of the optimized structures are given in Tables S2 and S3 in the Supporting Information.

Both the Fe^{III} centers are found to possess the following ground-state electronic configuration $(\delta_{xy})^1$ $(\pi^*_{yz})^1$ $(\pi^*_{xz})^1$ $(\delta_{x^2-y^2})^1$ $(\sigma^*_{z^2})^1$ (Figure 2). The magnetic coupling of complex **I** is computed by using the ground-state structure employing the standard protocol[36] and this gives a J value of -145.4 cm^{-1}.[37] There is a significant π-type interaction between the d_{xz} and d_{yz} orbitals of the two Fe centers through the μ-oxo bridge (see Table S4 in the Supporting Information) and this strong interaction leads to a strong antiferromagnetic coupling in this species. This is supported by the calculation of overlap integrals between the singly occupied molecular orbitals (see Table S4 in the Supporting Information). Comparison between the spin density plots computed for the $^{1}\mathbf{I}_{hs}$ and $^{11}\mathbf{I}_{hs}$ states (see Figure 1b and Figure S8 in the Supporting Information), reveals a dominant spin delocalization mechanism through which both the Fe^{III} centers are coupled. The μ-oxo oxygen is found to possess a spin density of 0.76 at the high-spin state, however, owing to cancellation of spins, at the ground state the μ-oxo oxygen possesses nearly zero spin density values. Significant spin densities on the carboxamido N and O atoms reveal that the magnetic exchange propagates not only through the μ-oxo bridge, but also through these bridges, offering a counter-complementarity effect leading to smaller antiferromagnetic exchange than what is expected for a bare μ-oxo bridged Fe^{III} dimer.[38]

The μ-oxo Fe–O bond of the $^{1}\mathbf{I}_{hs}$ state is found to be symmetric between the two Fe^{III} centers with a distance of 1.821 Å and the Fe–N_{avg} bond length is computed to be 2.180 Å (see Table S1 in the Supporting Information). The computed geometrical parameters are consistent with the X-ray structure reported[14b] and this offers confidence in the employed methodology. NBO analysis reveals that σ-bonding interaction in the Fe^{III}-μ-oxo bond is composed of 24.7% of Fe(1)-d_{z^2} and 75.3% of O(p_z*) orbitals (see Figure S1a in the Supporting Information), suggesting ionic character. The electronic configuration of the $^{1}\mathbf{I}_{hs}$ state reveals similar contributions between both iron-μ-oxo atoms.

To probe the electronic structure further and to compare it with experimental observations, we have computed the spectroscopic parameters of complex **I**. The TD-DFT computed absorption spectra using acetonitrile solvent for the $^{1}\mathbf{I}_{hs}$ state shows four features at 356, 402, 436, and 517 nm. Although the computed features are in broad agreement with the experimental features[39] (Figure 3), some deviations in the absolute values are noted. Benchmarking studies of the exchange-correlation functional for the prediction of absorption spectra reported such observations earlier for the B3LYP functional.[40] The peaks computed at 356 and 402 nm are found to be of ligand to metal charge-transfer transitions (Figure 3). The peak observed at 436 nm has a predominant d–d character where a α-(Fe1$_{dz^2}$)→α-(Fe2$_{dyz}$) transition is witnessed. Similarly, the peak at 517 nm corresponds to a β-(Fe2$_{dz^2}$)→β-(Fe1$_{dxy}$) transition. The computed isomer shift (δ) and quadrupole splitting $|\Delta E_Q|$ values for the $^{1}\mathbf{I}_{hs}$ state are $\delta=0.42$ mm s^{-1} and $\Delta E_Q=$

Table 1. Different possible spin state configurations of complex **I**.

Spin states	Electronic configuration Fe^{III}	Fe^{III}	Relative energy [kJ mol^{-1}]
$^{11}\mathbf{I}_{hs}$	$\delta^{\uparrow}_{xy}\,\pi^{*\uparrow}_{yz}\,\pi^{*\uparrow}_{xz}\,\delta^{\uparrow}_{x^2-y^2}\,\sigma^{*\uparrow}_{z^2}$	$\delta^{\uparrow}_{xy}\,\pi^{*\uparrow}_{yz}\,\pi^{*\uparrow}_{xz}\,\delta^{\uparrow}_{x^2-y^2}\,\sigma^{*\uparrow}_{z^2}$	25.0
$^{1}\mathbf{I}_{hs}$	$\delta^{\uparrow}_{xy}\,\pi^{*\uparrow}_{yz}\,\pi^{*\uparrow}_{xz}\,\delta^{\uparrow}_{x^2-y^2}\,\sigma^{*\uparrow}_{z^2}$	$\delta^{\downarrow}_{xy}\,\pi^{*\downarrow}_{yz}\,\pi^{*\downarrow}_{xz}\,\delta^{\downarrow}_{x^2-y^2}\,\sigma^{*\downarrow}_{z^2}$	0.0
$^{7}\mathbf{I}_{is}$	$\delta^{\uparrow\downarrow}_{xy}\,\pi^{*\uparrow}_{yz}\,\pi^{*\uparrow}_{xz}\,\delta^{\uparrow}_{x^2-y^2}\,\sigma^{*}_{z^2}$	$\delta^{\uparrow\downarrow}_{xy}\,\pi^{*\uparrow}_{yz}\,\pi^{*\uparrow}_{xz}\,\delta^{\uparrow}_{x^2-y^2}\,\sigma^{*}_{z^2}$	101.9
$^{1}\mathbf{I}_{is}$	$\delta^{\uparrow\downarrow}_{xy}\,\pi^{*\uparrow}_{yz}\,\pi^{*\uparrow}_{xz}\,\delta^{\uparrow}_{x^2-y^2}\,\sigma^{*}_{z^2}$	$\delta^{\uparrow\downarrow}_{xy}\,\pi^{*\downarrow}_{yz}\,\pi^{*\downarrow}_{xz}\,\delta^{\downarrow}_{x^2-y^2}\,\sigma^{*}_{z^2}$	101.2
$^{3}\mathbf{I}_{ls}$	$\delta^{\uparrow\downarrow}_{xy}\,\pi^{*\uparrow\downarrow}_{yz}\,\pi^{*\uparrow}_{xz}\,\delta_{x^2-y^2}\,\sigma^{*}_{z^2}$	$\delta^{\uparrow\downarrow}_{xy}\,\pi^{*\uparrow}_{yz}\,\pi^{*\uparrow\downarrow}_{xz}\,\delta_{x^2-y^2}\,\sigma^{*}_{z^2}$	125.2
$^{1}\mathbf{I}_{ls}$	$\delta^{\uparrow\downarrow}_{xy}\,\pi^{*\uparrow\downarrow}_{yz}\,\pi^{*\uparrow}_{xz}\,\delta_{x^2-y^2}\,\sigma^{*}_{z^2}$	$\delta^{\uparrow\downarrow}_{xy}\,\pi^{*\uparrow\downarrow}_{yz}\,\pi^{*\downarrow}_{xz}\,\delta_{x^2-y^2}\,\sigma^{*}_{z^2}$	178.6

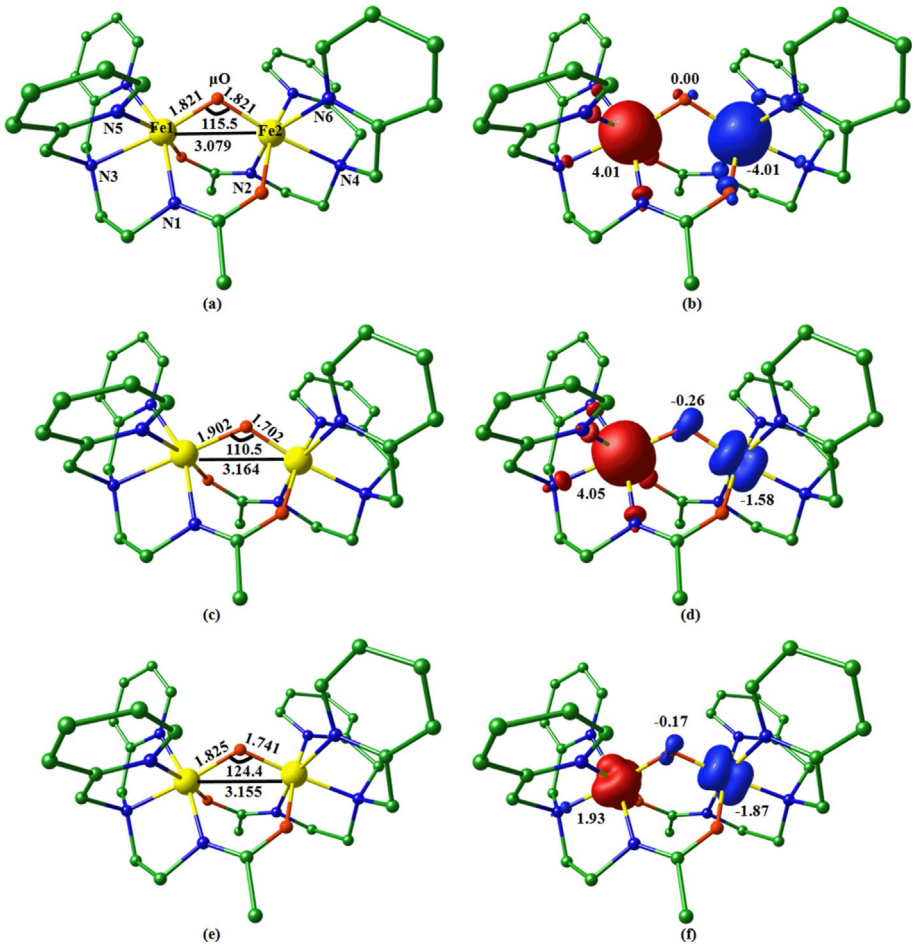

Figure 1. The optimized structure of: a) $^{1}\mathbf{I}_{hs}$, and b) its corresponding spin density plot. The optimized structure of: c) $^{4}\mathbf{II}_{hs\text{-}is}$, and d) its corresponding spin density plot. The optimized structure of: e) $^{1}\mathbf{III}_{is}$, and f) its corresponding spin density plot.

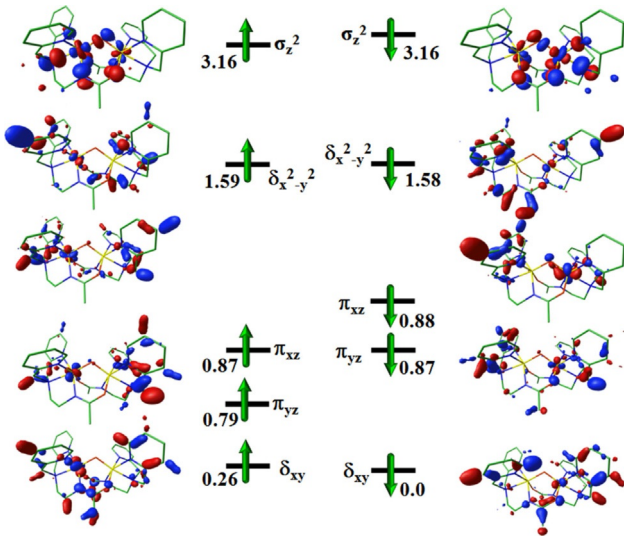

Figure 2. The computed Eigenvalue plot incorporating energies computed for d-based orbitals for alpha and beta spin corresponding to the ground state ($^{1}\mathbf{I}_{hs}$) of the complex **I** (energies are given in eV).

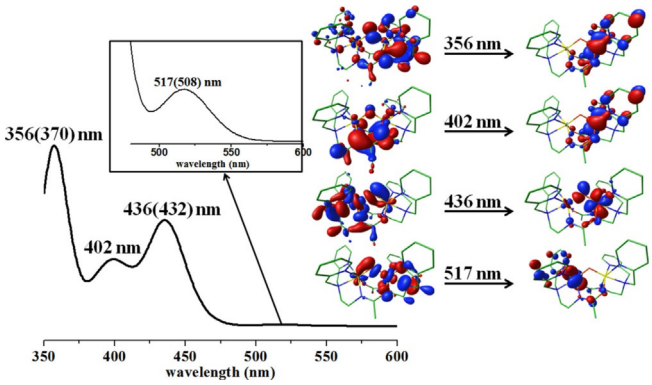

Figure 3. Absorption spectra computed by using TD-DFT calculations on the ground state of complex **I** and its corresponding orbitals involved in the transitions. The values given in parenthesis are the corresponding experimental values.

1.07 mm s^{-1}, respectively (Table 2) and are same for both the iron(III) centers. The computed parameters are in agreement with the experimental data and this clearly indicates that the observed spectral features can be rationalized based on the ground state structure. We would like to note here that the standard deviation expected for the α, β, and C parameters employed to compute the isomer shift is estimated to be 0.08 mm s^{-1} for the methodology employed.[34] To ascertain

Table 2. Computed spectroscopic parameters along with the experimental values reported for complexes **I–III**.

Complex	δ values [mm s^{-1}] exptl[14b]	calcd Fe(1)	calcd Fe(2)	ΔE_Q values [mm s^{-1}] exptl[14b]	calcd Fe(1)	calcd Fe(2)	J [cm^{-1}]
{Fe^{III}-μ(O)-Fe^{III}}	0.45	0.417	0.417	1.30	1.070	1.070	−145.4
{Fe^{III}-μ(O)-Fe^{IV}}	0.07	0.388	−0.034	1.57	0.540	1.808	−335.6
{Fe^{IV}-μ(O)-Fe^{IV}}	−0.05	−0.039	−0.041	2.14	2.914	2.225	−114.5

the accuracy of these calculations further, we have performed additional geometry optimizations and calculation of Mössbauer parameters by using the BP86 functional. The computed values using this methodology are given in the Supporting Information (Table S8); apparently, the values estimated by using this methodology are found to be inferior compared with the B3LYP estimation on comparison with the experimental parameters.

Additionally, our calculations suggest that the singlet ground state of complex **I** is derived from two high-spin Fe^{III} centers coupled in an antiferromagnetic fashion and rules out other two singlet state possibilities listed in Table 1.

Complex II {Fe^{III}-μ(O)-Fe^{IV}}

One-electron oxidation of complex **I** leads to the formation of complex **II**. For complex **II**, the ligand environment is similar for both iron centers but the electronic environments are different. Here, both metal centers are in different oxidation states and this leads to nine possible electronic combinations, which are denoted as ^{10}**II**$_{hs\text{-}hs}$, ^{2}**II**$_{hs\text{-}hs}$, ^{6}**II**$_{is\text{-}is}$, ^{2}**II**$_{is\text{-}is}$, ^{4}**II**$_{ls\text{-}is}$, ^{2}**II**$_{ls\text{-}is}$, ^{8}**II**$_{hs\text{-}is}$, ^{4}**II**$_{hs\text{-}is}$, and ^{2}**II**$_{ls\text{-}ls}$, respectively (see Table S5 in the Supporting Information). We have computed eight spin states and our results show that the ^{4}**II**$_{hs\text{-}is}$ quartet state is the ground state followed by ^{10}**II**$_{hs\text{-}hs}$, ^{2}**II**$_{hs\text{-}hs}$, ^{6}**II**$_{is\text{-}is}$, ^{2}**II**$_{is\text{-}is}$, ^{4}**II**$_{ls\text{-}is}$, ^{2}**II**$_{ls\text{-}is}$, and ^{8}**II**$_{hs\text{-}is}$ at 45.8, 27.6, 57.6, 49.0, 1.9, 7.3, and 23.4 kJ mol^{-1} energy, respectively. Here, it should be noted that owing to the self-consistent field (SCF) convergence problem, the ^{2}**II**$_{ls\text{-}ls}$ state could not be computed. Our calculations reveal that at the ground state, the Fe^{III} ion has high-spin configuration whereas the Fe^{IV} ion possesses intermediate spin configuration. Typical aminopyridine ligands generally stabilize the intermediate spin state as the ground state for Fe^{IV}-oxo species and this is due to strong σ-antibonding interaction with the d_{z^2} orbital.[3c,21,41] Our computed results are in agreement with this expectation and it is also supported by the experimental studies performed earlier on the mixed valance oxo bridged iron dimers.[16,42]

The μ-oxo bridge mediates a strong delocalization of spin, leading to an antiferromagnetic coupling between the two metal centers resulting in the stabilization of the $S=3/2$ (^{4}**II**$_{hs\text{-}is}$) state as the ground state.[16] The optimized geometry and the spin density plot of the ground state of complex **II** are shown in Figure 1 c and d (see Table S1 in the Supporting Information for all the spin state structural parameters). The electronic configuration of the Fe^{III} center is computed to be $(\delta_{xy})^1$ $(\pi^*_{xz})^1$ $(\pi^*_{yz})^1$ $(\delta_{x^2-y^2})^1$ $(\sigma^*_{z^2})^1$ whereas the Fe^{IV} center is computed to be $(\delta_{xy})^2$ $(\pi^*_{yz})^1$ $(\pi^*_{xz})^1$ $(\delta_{x^2-y^2})^0$ $(\sigma^*_{z^2})^0$ for the **II**$_{hs\text{-}is}$ state (see Figure S2 in the Supporting Information). The Eigenvalue plot of the ^{4}**II**$_{hs\text{-}is}$ state reveals that the energy gap between the t_{2g} and e_g orbitals in case of the Fe^{III} center is computed to be smaller compared with the very high energy gap observed in case of the Fe^{IV} center. The shorter Fe^{IV}–μO bond compared with the Fe^{III}–μO bond facilitates stronger σ-interaction and uncovers the reason for the differential spin character observed between the two Fe centers.

The magnetic coupling constant (J) of complex **II** at the ground state is estimated to be −335.6 cm^{-1}. The strong antiferromagnetic interaction arises from the dominant π-type $d_{yz}|p_y|d_{yz}$ overlap between the two iron centers (see Table S6 in the Supporting Information). For the ^{4}**II**$_{hs\text{-}is}$ state, the spin density on the Fe^{III} center is estimated to be 4.05 whereas the spin density on the Fe^{IV} center is estimated to be −1.58 and a significant spin density (−0.26) on the Fe-μ-oxo is also observed (Figure 1 d). The spin density plot (Figure 1 d) clearly reveals a significant negative spin density at the μ-oxo bridge but the magnitude is less than what is generally expected for a ferryl oxygen atom of the monomeric Fe^{IV}=O unit. Both the Fe^{III} and Fe^{IV} centers are promoting spin delocalization with the oxygen atom, leading to cancellation of spins and reduction of radical character at the μ-oxo bridge (see Table S3 in the Supporting Information). The two Fe^{III}–μO and Fe^{IV}–μO bond lengths of the ^{4}**II**$_{hs\text{-}is}$ state are computed to be 1.902 and 1.702 Å, respectively. This large difference in bond lengths reflects a single bond between Fe^{III} and oxygen whereas Fe^{IV}=μO maintains double bond character. This is clearly witnessed in the computed Wiberg bond (WB) indices (0.9 and 0.7 for Fe^{IV}=μO and Fe^{III}–μO species, respectively). The Fe^{IV}=μO bond lengths are approximately 0.1 Å longer compared with the monomeric Fe^{IV}=O species.[3c,14b,21] NBO analysis of the Fe^{III}–μ-oxo bond shows it is composed of 18.5% Fe(1)-d_{z^2} and 81.5% O(p_z*) orbitals (Figure S1 b in the Supporting Information). For the Fe^{IV}=μO bond, the composition is 30.5% Fe(2)-d_{z^2} and 69.5% O(p_z*) orbitals for the σ-bond, whereas 37.4% from Fe2 and 62.6% from μO contributes for the π-bond. Owing to the difference in the oxidation state, there is a significant variation in Fe–O bonding as reflected in the computed bond ionicity[43] (0.9 for the Fe^{III}–μO vs. 0.67/0.47 for the σ/π bond in Fe^{IV}=μO).

The computed absorption spectra of the ground state ^{4}**II**$_{hs\text{-}is}$ are shown in Figure S3 in the Supporting Information. TD-DFT calculations give five intense absorption peaks at 416, 433, 490, 542, and 667 nm (see Figure S3 in the Supporting Information). Experimentally, a peak at 550 nm and a broad peak centered around 878 nm are detected. Interestingly, significant number of bands are noted in the very low energy region (below 1050 nm) and some of them correspond to intervalance charge-transfer bands (IVCT).[44] However, as the experimental spectra were not recorded beyond 1050 nm, predicted features beyond this wavelength could not be verified (see Figure S4 in the Supporting Information). Two sets of δ and $|\Delta E_Q|$ parameters are noted for this complex corresponding to Fe^{III} and Fe^{IV} oxidation states (Table 2). The δ value of 0.39 mm s^{-1} is computed for the Fe^{III} center whereas −0.03 mm s^{-1} is computed for the Fe^{IV} center. Experimentally, however, only one set of pa-

rameters is reported and this is in agreement with the computed Fe^{IV} center parameters but not the Fe^{III} center. In fact, experimental observation of only one isomer shift suggests a valance delocalization whereas our calculations suggest an asymmetric valance localized picture. Although valance localized asymmetric Fe^{III}-O-Fe^{IV} intermediates are reported for class 1a RNAs enzyme[45] and other bio-mimic models,[17c] we would like to judge how far the symmetric structure is maintained in terms of energy for species **II** as revealed by the Mossbauer data. To estimate this, we have performed additional calculations, where we have fixed the μ-O bonds symmetric between the Fe^{III} and Fe^{IV} atoms at 1.80 Å and this geometry is found to be only 1.2 kJ mol^{-1} higher in energy compared with the ground state structure, suggesting subtle energy differences between the symmetric and asymmetric structures of this species.

In addition, the computed energetics reveal the presence of several spin states within a 10 kJ mol^{-1} energy window and some of these states exhibit valance delocalization (see Table S3 in the Supporting Information). Our energetics and spectral data reveal the $S=3/2$ state observed for this species arises from the antiferromagnetic coupling of hs Fe^{III} and is spin Fe^{IV} centers[16] and not from other possibilities mentioned in the Table S3 in the Supporting Information.

Complex III {Fe^{IV}-μ(O)-Fe^{IV}}

Further one-electron oxidation of complex **II** generates complex **III**. Complex **III** possess identical spin on each Fe atom as they are associated with the same electronic environment, similar to complex **I**. Here, five different possible spin states, ^{9}**III**$_{hs}$, ^{1}**III**$_{hs}$, ^{5}**III**$_{is}$, ^{1}**III**$_{is}$, and ^{1}**III**$_{ls}$, are considered and the electronic configurations for each of the Fe atoms are schematically shown in Table S7 in the Supporting Information. Our DFT calculations reveal the ^{1}**III**$_{is}$ state as the ground state for this species. Other spin states such as ^{9}**III**$_{hs}$, ^{1}**III**$_{hs}$, ^{5}**III**$_{is}$, and ^{1}**III**$_{ls}$ lie 81.5, 61.8, 2.5, and 190.8 kJ mol^{-1} higher in energy, respectively. Experimental spectra clearly reveal an $S=0$ ground state arising from individual $S=1$ states from the Fe^{IV} centers and this strongly supports our calculations.[14b]

Here, both the Fe^{IV} centers have the same ground state electronic configuration of $(\delta_{xy})^2$ $(\pi^*_{yz})^1$ $(\pi^*_{xz})^1$ $(\sigma^*_{z^2})^0$ $(\delta_{x^2-y^2})^0$ (see Figure S5 in the Supporting Information). The magnetic exchange between the two Fe^{IV} centers is estimated to be antiferromagnetic in nature with a J value of -114.5 cm^{-1}. Although an experimental J value for complex **III** is not reported, the {Fe^{IV}_2(μ-O)$_2$} core reported earlier possesses a J value of -80 cm^{-1} and this is smaller than the computed J value of complex **III**, which is in agreement with our expectation. This interaction is strongly supported by the overlap integral calculation of the ^{1}**III**$_{is}$ state, which reveals a significant $d_{yz}|p_x|d_{xz}$ interaction between the two iron centers (see Table S6 in the Supporting Information). The spin density plot (Figure 1f) also suggests a significant spin polarization along the iron-μO-iron atoms. The optimized structure of the ground state of complex **III** (^{1}**III**$_{is}$) is shown in Figure 1e. The Fe(1)–μ-oxo and the Fe(2)–μ-oxo bond lengths are computed to be 1.825 and 1.740 Å, respectively (see Table S2 in the Supporting Information). The WB index values for both Fe^{IV}–μ-oxo bonds are computed to be 0.7 and 0.9. Additionally, our calculations clearly reveal that although both the iron centers have equivalent formal charge, there is a significant difference in Fe–O bond lengths. Iron atom possessing beta electrons (the negative spin density in Figure 1f) has shorter Fe–O bond lengths compared with the other Fe atom. NBO analysis reveals similar σ-bonding effects between the two iron atoms, (Fe1/Fe2 18.6/19.4%; O1/O2 81.4/80.6%, Figure S1c in the Supporting Information). However, the Fe(2)–μ-oxo possesses additional Fe–O π-bond character where 30.3% contribution from Fe(2) and 63.7% contribution from the bridged O atoms are detected. This suggests a Fe^{IV}–μO=Fe^{IV} type of bonding for the ground state of complex **III**. These significant differences in bonding and polarization of the μ-oxo group led to the observed catalytic behavior towards C–H/O–H bond activation.

The X-ray structure of complex **III** is not available, however, extended X-ray absorption fine structure (EXAFS) analysis on complex **III** suggests the Fe–Fe distance to be 3.08 Å and the average Fe–O distance is estimated to be 1.71 Å. Calculations yield an average Fe–O distance of 1.78 Å and comparison of these two values suggest that the Fe–O bond lengths are slightly overestimated by the calculations.[14b] Compared with the di-μ-oxo-diiron(IV) species reported earlier, where the presence of two μ-oxo groups yield a symmetric Fe^{IV}-oxo environment,[14c] here, our calculations suggest an asymmetric environment with one shorter and one longer Fe–O bond owing to the presence of one μ-oxo group.

The computed absorption spectra of the ground state (^{1}**III**$_{is}$) is shown in Figure 4. TD-DFT calculations predict three intense absorption peaks at 460 nm, 534 nm, and 611 nm (see Figure 4 and Figure S6 in the Supporting Information).[14b] The intense peak at 460 nm corresponds to ligand (N-ligand) to metal (π* (d_{xz}–p_x) orbital) charge-transfer transitions. The computed feature at 534 nm corresponds to a α-(Fe2$_{dxy}$)→α-(Fe1$_{dz^2}$) transition whereas the one observed at 611 nm corresponds to the ligand to metal charge-transfer band. Experimentally, one distinct absorption peak at approximately 550 nm was recorded for complex **III** and reduction of complex **III** to complex **II** by 0.1 M cyclohexane revealed some hidden features at approxi-

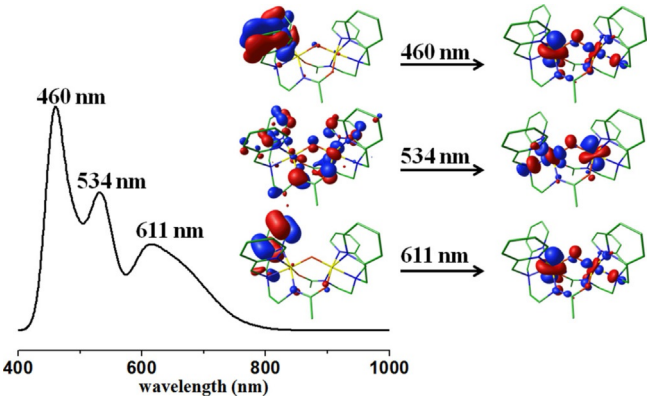

Figure 4. The TD-DFT computed absorption spectra for the complex (^{1}**III**$_{is}$) and the corresponding orbitals involved in the transitions.

mately 650 nm. Although the calculated bands are underestimated compared with the experiments, the features observed in the experimental spectra are reproduced in the calculations.

The isomer shift (δ) and quadrupole splitting $|\Delta E_Q|$ parameters of the ground state (^{1}**III**$_{is}$) of complex **III** are computed to be −0.04 (−0.04) mm s^{-1} and 2.91 (2.23) mm s^{-1} for the Fe1 (Fe2) center (Table 2). Experimentally, only one set of values is obtained upon simulation of spectra for an $S=0$ coupled state. Very close resemblance of computed data to the experiments[14b] supports the $S=1$ Fe(1) and $S=1$ Fe(2) centers coupled in an antiferromagnetic fashion leading to ^{1}**III**$_{is}$ as the ground state. This is similar to the ground state estimated for the diamond core $[Fe^{IV}_2(\mu\text{-}O)_2]^{4+}$ unit observed in sMMO and other bio-mimic models.[9d,14a,46] Calculations correctly predict the variation in the δ value as we move from complex **I** to **III**.

Reactivity of complex III {Fe^{IV}-μ(O)-Fe^{IV}} towards C–H and O–H bond activation

After the detailed electronic investigation of the complexes **I**–**III**, we were interested in probing the mechanism of the C–H and O–H bond activation and reactivity trends with complex **III**. Monomeric iron(IV)-oxo complexes are popular oxidants for several catalytic transformation reactions[47] but, recently, dinuclear iron complexes have picked up the pace and in some cases have been found to be stronger oxidants than the corresponding mononuclear complexes.[8f,14b,18,48] The high redox potential of complex **III** among the three complexes (**I**–**III**) reveals that it is a powerful oxidant.[14b] Complex **III** was found to activate C–H bonds as strong as 400 kJ mol^{-1} and found to react 1000 times faster than a mononuclear Fe^{IV}=O complexes.[14b] Although C–H bond activation by monomeric iron(IV)-oxo species are known,[49] activation of a very strong O–H bond has no precedence.[14b] Quite interestingly, these species are found to cleave O–H bonds of methanol and *tert*-butanol selectively instead of their weaker C–H bonds. One species possessing dual catalytic abilities depending on the nature of the substrate is rare and this has motivated us to probe the electronic and mechanistic origin of the reactivity of complex **III**. Here, we have undertaken a detailed study to explore the mechanism of the formation of acetone from tertiary butyl alcohol (*tert*-butanol) and cyclohexene from cyclohexane by using complex **III**.

Hydrogen atom abstraction of cyclohexane

Based on the experimental evidence and earlier theoretical studies,[8f,14b,47a,50] we have adapted the following mechanism for the dehydrogenation of cyclohexane (Scheme 2). In the first step, the bridged oxygen complex **III** abstracts a hydrogen

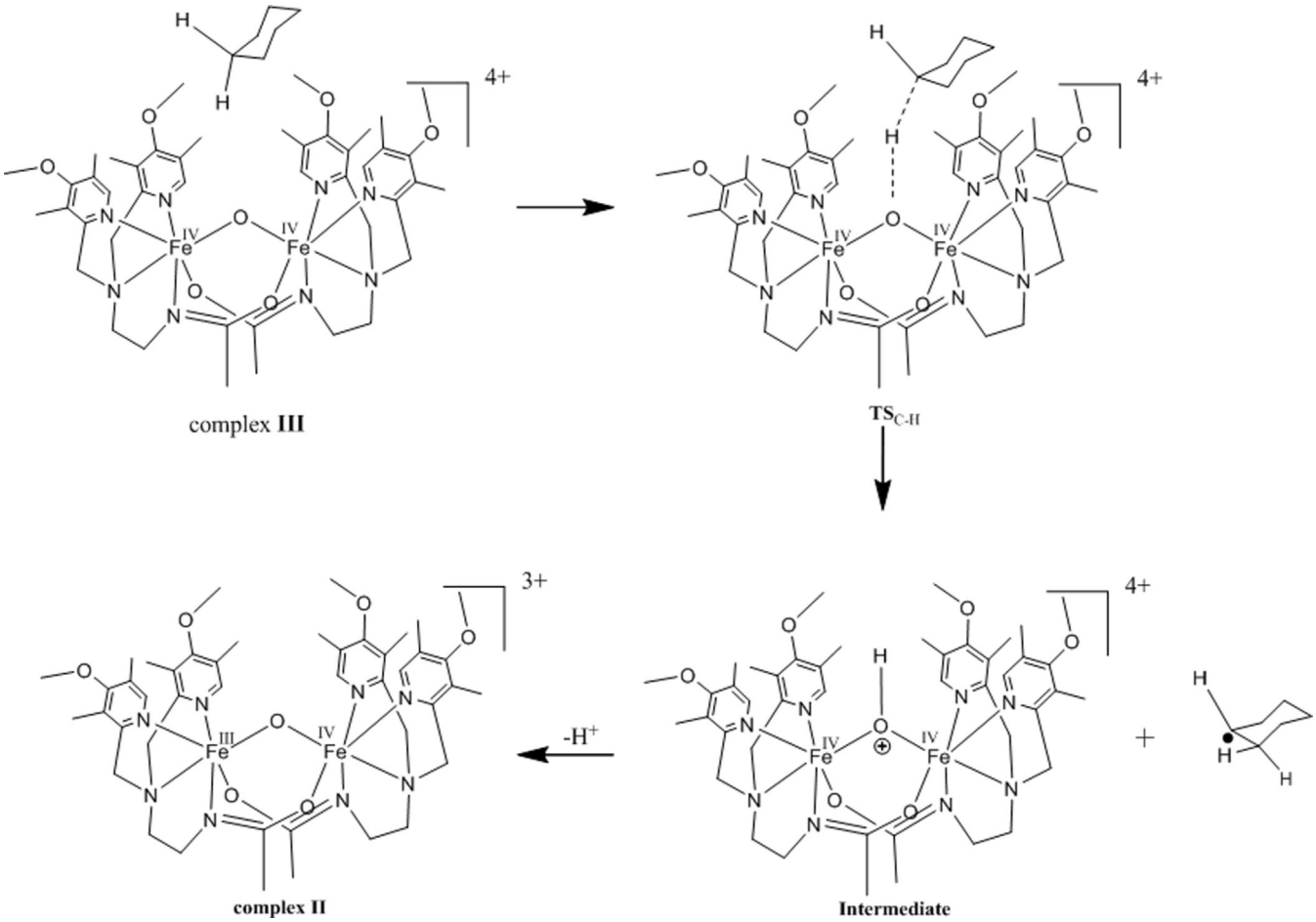

Scheme 2. The schematic mechanism of C–H activation of cyclohexane by complex **III** {Fe^{IV}-O-Fe^{IV}}.

atom from the cyclohexane via transition state $\mathbf{TS_{C\text{-}H}}$ and forms a cyclohexyl radical along with the {Fe^{III}-μO(H)-Fe^{IV}} intermediate. Another hydrogen atom abstraction from the cyclohexyl radical leads to the formation of cyclohexene.[51] Several reports on monomeric complexes reveal that the second hydrogen abstraction process has a smaller barrier height and hence we have restricted our calculations to the first step.[8f,52] An attempt has been made to calculate the $\mathbf{TS_{C\text{-}H}}$ on all spin surfaces and we have successfully computed the $^{9}\mathbf{TS_{C\text{-}Hhs}}$, $^{1}\mathbf{TS_{C\text{-}Hhs}}$, $^{5}\mathbf{TS_{C\text{-}His}}$, and $^{1}\mathbf{TS_{C\text{-}His}}$ transition states although $^{1}\mathbf{TS_{C\text{-}Hls}}$ could not be obtained (the $^{1}\mathbf{III_{ls}}$ spin state lies 229.1 kJ mol^{-1} higher in energy than the $^{1}\mathbf{III_{is}}$ ground state and thus it may not be a relevant spin state in this reaction scenario). Our computed results show $^{9}\mathbf{TS_{C\text{-}Hhs}}$ to be the lowest lying with a barrier height of 126.4 kJ mol^{-1} whereas the $^{5}\mathbf{TS_{C\text{-}His}}$ transition state lies at 147.2 kJ mol^{-1}. Lower barrier heights for the $^{9}\mathbf{TS_{C\text{-}Hhs}}$ species suggest a possible two/multi-state reactivity scenario for this species.[21,53] The barrier heights computed incorporating only the ZPE corrections are given in the Supporting Information (Figure S9).

The $^{1}\mathbf{TS_{C\text{-}Hhs}}$ and $^{1}\mathbf{TS_{C\text{-}His}}$ are found to be 201.5 and 355.1 kJ mol^{-1} in energy, respectively, and thus are unlikely to participate in the reaction mechanism (Figure 5). Interestingly,

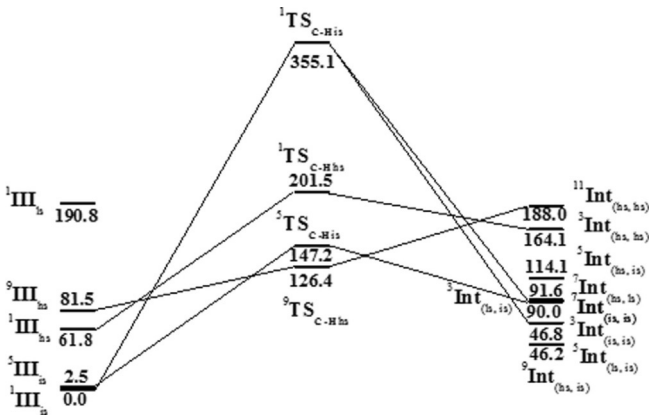

Figure 5. B3LYP-D3 computed potential energy surface for C–H bond activation of cyclohexane by complex **III** (Δ*G* in kJ mol^{-1}).

the ground state of complex **III** is the $^{1}\mathbf{III_{is}}$ species possessing $S=1$ on both the Fe^{IV} centers, but the transition state corresponding to this spin state is prohibitively high (355.1 kJ mol^{-1}) for participation in the reaction mechanism. The $^{5}\mathbf{III_{is}}$ and $^{9}\mathbf{III_{hs}}$ spin states of complex **III**, lying at 2.5 and 81.5 kJ mol^{-1}, are found to offer lower energy pathways at the transition state. The $^{1}\mathbf{III_{is}} \rightarrow {}^{9}\mathbf{TS_{C\text{-}Hhs}}$ path suggests that the reaction proceeds through a minimum energy crossing point (MECP).[26] The majority of the mononuclear Fe^{IV}-oxo complexes are found to react via the quintet first excited state and in many instances, the MECPs are found to be energetically favorable[6b,54] and in least at two instances, exclusively spin–orbit coupling has been incorporated to validate the possible spin crossover.[55] For the $^{1}\mathbf{III_{is}} \rightarrow {}^{5}\mathbf{TS_{C\text{-}His}}$ pathway, although the multiplicity changes, the energy here corresponds to the exchange-coupling between the two Fe^{IV} centers and the switch from antiferromagnetic coupling to ferromagnetic coupling is sufficient to effect this pathway. As the sign of magnetic coupling is correlated to the Fe–O distance and the Fe-μO-Fe angles, this can be rather easily achieved during the structural transformations. Note that Fe–O distances and Fe-μO-Fe bond angles are significantly different in the transition state compared with that of the reactant (see Table S2 in the Supporting Information).

The optimized structures of $^{9}\mathbf{TS_{C\text{-}Hhs}}$ and $^{5}\mathbf{TS_{C\text{-}His}}$ for the C–H bond activation are shown in Figure 6a and c, respectively. For the $^{9}\mathbf{TS_{C\text{-}Hhs}}$ species, the Fe(1)–μO and Fe(2)–μO bond lengths are elongated to 2.071 and 1.806 Å from 1.825 and 1.741 Å, respectively (see Table S1 in the Supporting Information). The μO-H-C(cyclohexane) bond angle is determined to be 172.1° whereas the Fe(2)-μO-H/Fe(1)-μO-H angles are determined to be 117.7/122.4°. Interestingly, the α-HOMO of this transition state reveals a π-type pathway with the Fe(2) center and a σ-type pathway with the Fe(1) center (Figure 7a). Unlike in mononuclear Fe^{IV}-oxo complexes, where the μO-H-C(cyclohexane) angle determines the nature of the σ/π pathway,[8f,56] the Fe-μO-H angle plays a critical role here in the dinuclear framework as linear H-μO-Fe are impossible to attain owing to structural restrictions. In mononuclear Fe^{IV}-oxo complexes, the σ pathway via the $S=2$ surface is generally found to be low lying in energy whereas a flexible σ_{Fe1}–π_{Fe2} pathway is found to be operational here.

The computed spin density plot of the transition state is shown in Figure 6b. The Fe(1) center has a spin density of 4.10, whereas the Fe(2) center has a spin density of 1.83 and the substrate cyclohexane is also found to possess significant positive spin density. This suggests a β-electron transfer from the substrate to the d_{xy} orbital of the Fe(2) center accompanied by an internal α-electron transfer (IET) from Fe(2) to Fe(1) to attain the +3 oxidation state at Fe(1) (Scheme 3). The observed σ–π pathway, in fact, facilitates this transfer. An alternative way to achieve this electronic configuration includes α-electron transfer from the substrate to Fe(1) followed by pairing of the electrons at the Fe(2) center. This can be ruled out as the spin paring energy of the Fe^{IV} centers are generally large and such a mechanism should yield a negative spin density at the cyclohexane moiety in the transition state. Thus, the proposed mechanism consists of a proton-coupled electron transfer (PCET) process from the substrate,[57] accompanied by an unusual internal electron rearrangement from Fe(1) to Fe(2). This is possible only in a dinuclear species and rationalizes why the presence of two metal ions promotes reactivity nearly 1000 times faster than monomeric Fe^{IV}-oxo complexes. We would like to note here that another pathway, electron transfer to the d_{xy} orbital, is termed as the δ pathway.[56a,57b] However, the frontier MOs that are involved in the electron transfer paths are clearly σ and π on both centers and suggest an internal rearrangement of electrons in the intermediate species. Although precedent for this mechanism has not been noted, recently a pentanuclear Fe-oxo complex was found to split water efficiently in which a {Fe^{IV}-μO-Fe^{IV}} type moiety is expected to be generated through an internal electron transfer from one metal center to another.[58] As this is a key mechanistic observation in the pentanuclear Fe reaction, this suggests the

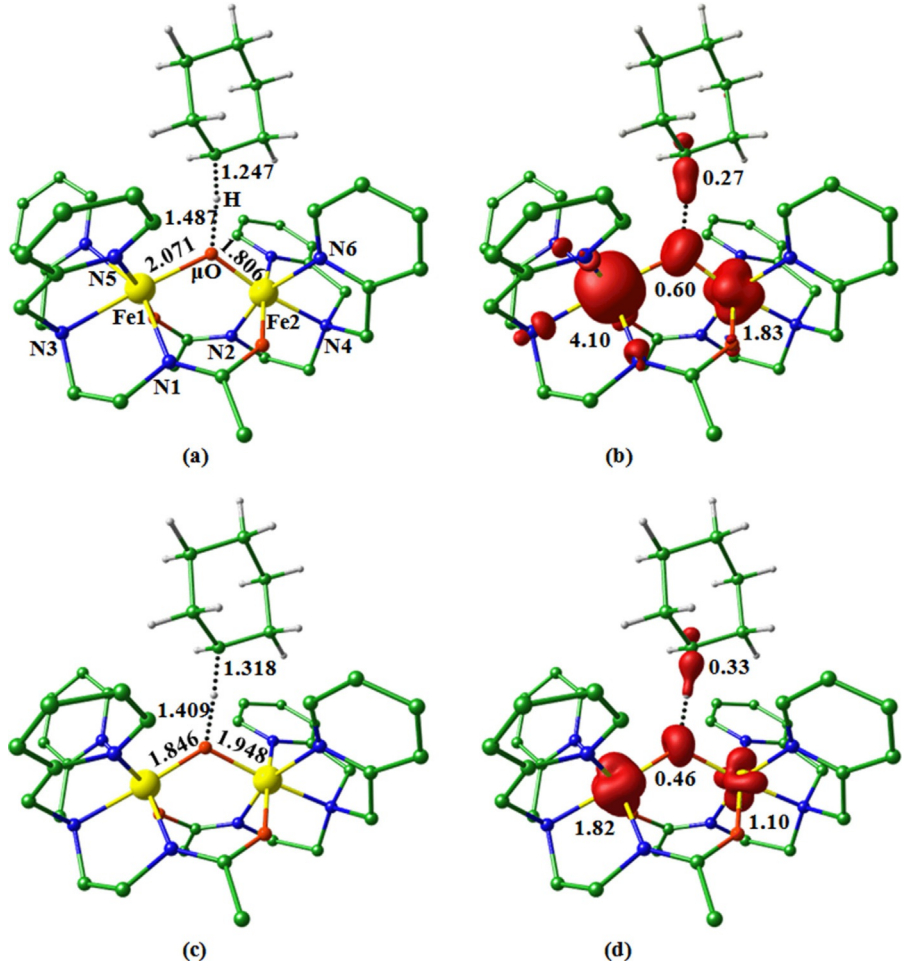

Figure 6. The optimized structure of: a) ^{9}**TS**$_{C\text{-}Hhs}$, and b) its corresponding spin density plot. The optimized structure of: c) ^{5}**TS**$_{C\text{-}His}$, and d) its corresponding spin density plot.

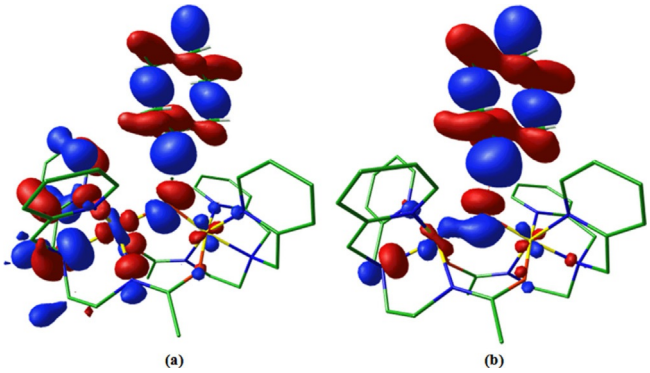

Figure 7. The computed HOMOs of the ^{9}**TS**$_{C\text{-}Hhs}$ and ^{5}**TS**$_{C\text{-}His}$ transition states for the C–H bond activation.

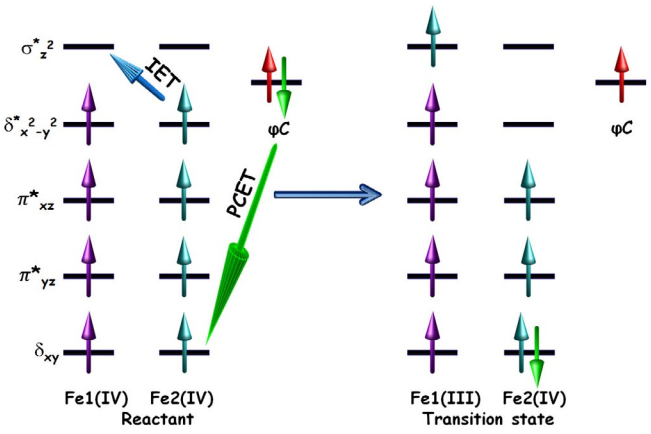

Scheme 3. The schematic orbital evolution diagram for the C–H activation of the ^{9}**TS**$_{C\text{-}Hhs}$ transition states. Here, IET describes an internal electron transfer from Fe^{IV} to another Fe^{IV} unit. PCET describe the proton-coupled electron transfer.

possibility of observing such features in reactions catalyzed by tetranuclear complexes.[58–59] Such electron transfer processes are also associated with the structural variation and entropic contributions to the barrier height and thus are likely to play a role here. To further probe the variation in entropy change, we have analyzed the variation in entropy across the structures studied (see Tables S11 and S12 in the Supporting Information). Although the computed variations are small, the entropy factor is found to favor the transition state and this is particularly true for states possessing several unpaired spins compared with other states with paired spins.

For the $^{5}\mathbf{TS}_{\mathbf{C\text{-}H}is}$ state, the Fe(2)-μO-H/Fe(1)-μO-H angles are determined to be 111.3/128.5°. The orbital analysis indicates a σ-pathway with the Fe(1) center and a π-pathway with the Fe(2) center, leading to the σ_{Fe1}–π_{Fe2} pathway for this species (Figure 7b). The spin density reveals β-electron transfer from the substrate to the Fe(2) center. This leads to a significant reduction of spin density on the Fe(2) center (from 1.61 to 1.10). As the Fe^{IV} center here are in the $S=1$ state, no internal electron transfers are observed and the spin density of the Fe(1) remains similar to that of the reactant.

Hydrogen atom abstraction results in the formation of the {Fe^{III}-μ(OH)-Fe^{IV}} intermediate. Considering the exchange between iron centers, there are ten possible spin states for this species ($^{11}\mathbf{Int}_{(hs,hs)}$, $^{3}\mathbf{Int}_{(hs,hs)}$, $^{7}\mathbf{Int}_{(is,is)}$, $^{3}\mathbf{Int}_{(is,is)}$, $^{3}\mathbf{Int}_{(ls,ls)}$, $^{7}\mathbf{Int}_{(hs,ls)}$, $^{5}\mathbf{Int}_{(ls,is)}$, $^{9}\mathbf{Int}_{(hs,is)}$, and $^{3}\mathbf{Int}_{(ls,is)}$). However, we are unable to converge intermediate $^{3}\mathbf{Int}_{(ls,ls)}$ to the desired solution. All the intermediates are computed to be slightly endothermic with respect to the reactant. The $^{9}\mathbf{Int}_{(hs,is)}$ state is found to be the lowest lying at 46.2 kJ mol^{-1} with respect to the reactant, followed by the $^{5}\mathbf{Int}_{(is,is)}$ state at 46.8 kJ mol^{-1}. Experimentally, the protonated species is found to lose the proton, readily leading to complex **II**. We have estimated the energetic requirement to be 5.9 kJ mol^{-1} for this reaction when using water and a hydronium ion, suggesting thermoneutral conditions. If larger water clusters are employed, they are likely to yield exothermic conditions.[6b] The proposed mechanism is consistent with experimental data where the kinetic isotopic effect (KIE) for the C–H bond activation of cyclohexane is estimated to be 3.5 and the second-order rate constant is determined to be $8.1\times10^{-2}\,\text{M}^{-1}\,\text{s}^{-1}$.[14b] Both of these numbers suggest the hydrogen abstraction of cyclohexane as the rate-determining step (rds) as is evident from our computations.

Mechanism of oxidation of tert-butanol by complex III

The experimental study shows that deuteration of the O–H bond results in a kinetic isotope effect (KIE) of 1.4–1.5 although no such observation has been noticed with the deuteration of C–H bonds.[14b] This suggests that the oxidation of *tert*-butanol occurs through O–H bond cleavage rather than C–H bond cleavage and the O–H bond cleavage is the rds.[14b] Based on the experimental data, we have proposed the following mechanism for the oxidation of *tert*-butanol (Scheme 4) by complex **III**.[14b] The bridged oxygen atom (μ-oxo) of complex **III** {Fe^{IV}-μO-Fe^{IV}} activates the O–H bond of the *tert*-butanol via transition state $\mathbf{TS}_{\mathbf{O\text{-}H}}$ (Scheme 4), where essentially the bridged oxygen abstracts the hydrogen atom, forming a *tert*-butoxide species and {Fe^{IV}-μO(H)-Fe^{III}} intermediate.[14b,60] This intermediate undergoes deprotonation to yield complex **II** as discussed earlier for the C–H bond activation mechanism. We have suc-

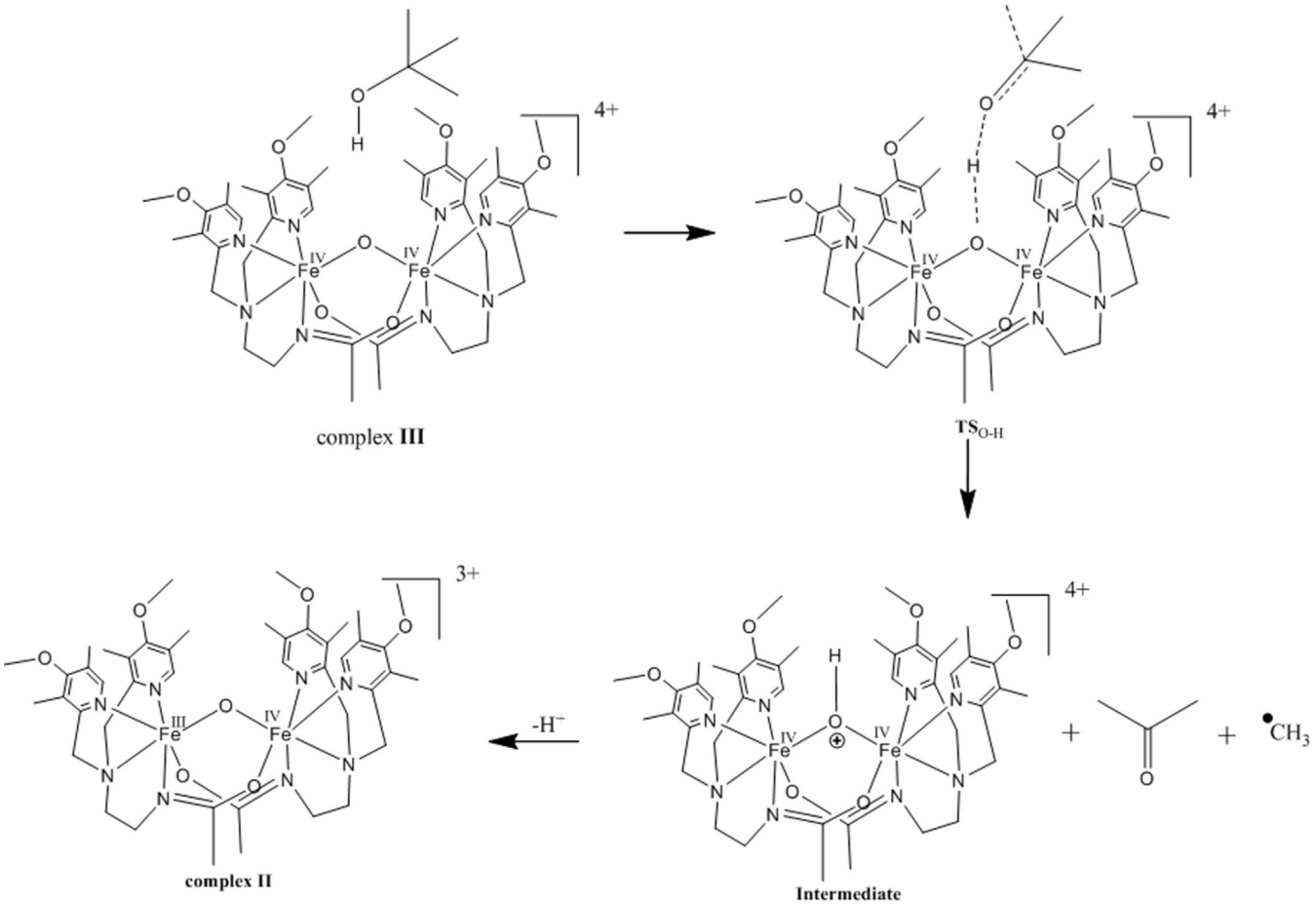

Scheme 4. The schematic mechanism of oxidation of *tert*-butanol by complex **III** {Fe^{IV}-O-Fe^{IV}}.

cessfully optimized all five possible transition states, $^{9}TS_{O\text{-}Hhs}$, $^{1}TS_{O\text{-}Hhs}$, $^{5}TS_{O\text{-}His}$, $^{1}TS_{O\text{-}His}$, and $^{1}TS_{O\text{-}Hls}$. The $^{5}TS_{O\text{-}His}$ transition state is computed to be lowest in energy and its barrier height is found to be 118.2 kJ mol^{-1} (Figure 8) followed by 150.9, 152.0, 200.7, and 340.0 kJ mol^{-1} for $^{1}TS_{O\text{-}His}$, $^{9}TS_{O\text{-}Hhs}$, $^{1}TS_{O\text{-}Hhs}$, and $^{1}TS_{O\text{-}Hls}$, respectively. The barrier heights computed incorporating only the ZPE corrections are given in the Supporting Information (Figure S10). The optimized structure of the transition state $^{5}TS_{O\text{-}His}$ is shown in Figure 9a. The computed bond lengths of $^{5}TS_{O\text{-}H}$ suggest that the distance between μ-oxo and the alcoholic hydrogen atom decreases to 1.737 Å along with the reduction of the length of the C–O in the *tert*-butanol moiety from 1.473 to 1.420 Å (see Table S1 in the Supporting Information). This suggests possible double bond character for the C–O bond. The H–O bond length of the hydroxyl group increases from 0.979 to 1.021 Å and simultaneously the C–C bond also elongates from 1.535 to 1.652 Å in the transition state. These parameters suggest that cleavage of O–H and the C–C bonds take place simultaneously and it is a product-like transition state. Frequency calculations clearly reveal that both the O–H and C–C bond cleavages are synchronous and to further verify the nature of the transition states, we have performed intrinsic reaction coordinate (IRC) calculations, which support our argument. The O-H-O bond angle of the transition state $^{5}TS_{O\text{-}His}$ is computed to be 149.9° and the Fe(1)-μO-H/Fe(2)-μO-H angles are determined to be 131.9/106.8°. The computed spin density plot of the $^{5}TS_{O\text{-}His}$ species (Figure 9b) suggests a β-electron transfer from the substrate to the d_{yz} orbital of the Fe(1) center to attain the +3 oxidation state (see Scheme S1 in the Supporting Information) and suggests π–π type pathway (see Table S3 and Figure S7 in the Supporting Information). A significant spin density on both the alcoholic oxygen ($\rho = 0.43$) and the carbon atom ($\rho = 0.21$) of the alkyl

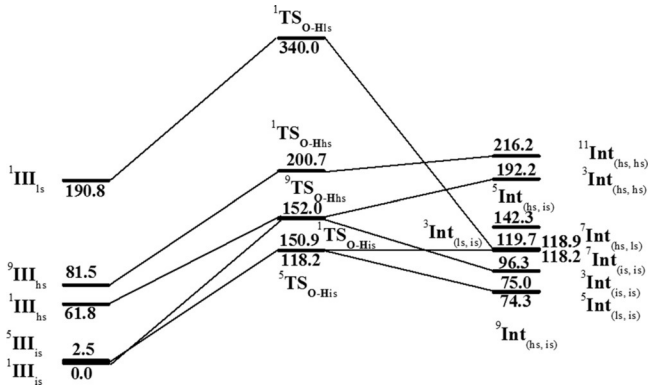

Figure 8. B3LYP-D3 computed potential energy surface for the O–H bond activation of *tert*-butanol by complex **III** (ΔG in kJ mol^{-1}).

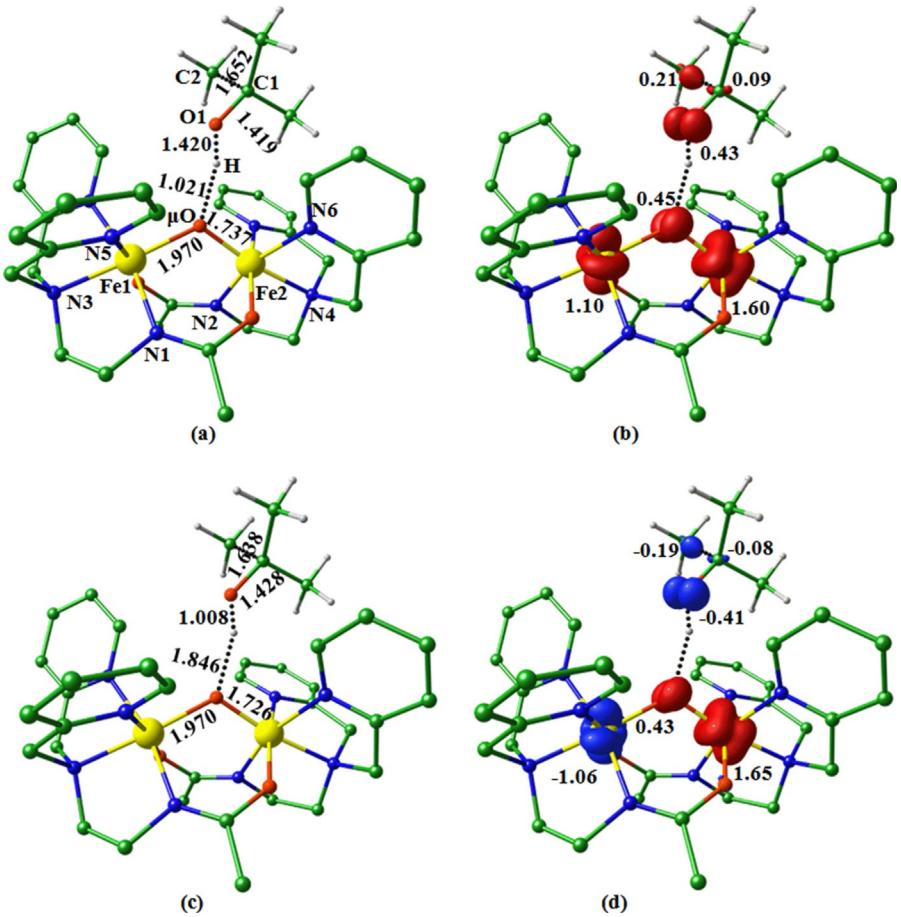

Figure 9. B3LYP-D3 computed the optimized structure of: a) $^{5}TS_{O\text{-}His}$, and b) its corresponding spin density plot. The optimized structure of: c) $^{1}TS_{C\text{-}His}$, and d) its corresponding spin density plot.

group reveals that this oxidation takes place through a radical pathway rather than a cationic or anionic (Figure 9b) pathway. From the spin density analysis, we can conclude that this reaction can take place through a proton-coupled electron transfer mechanism (see Scheme S2 in the Supporting Information). The next closest (at 103.2 kJ mol^{-1}) lying transition state is ^{1}**TS**$_{O\text{-}His}$ (Figure 9c and d) corresponding to the antiferromagnetic solution of the ^{5}**TS**$_{O\text{-}His}$ species discussed earlier. For the ^{1}**TS**$_{O\text{-}His}$ state, the Fe(1)-μO-H/Fe(2)-μO-H angles are determined to be 133.6/105.2°. Here, a α-electron transfer from the substrate to the Fe(1) center has been observed with a π–π type pathway (see Figure S7 and Scheme S2 in the Supporting Information).

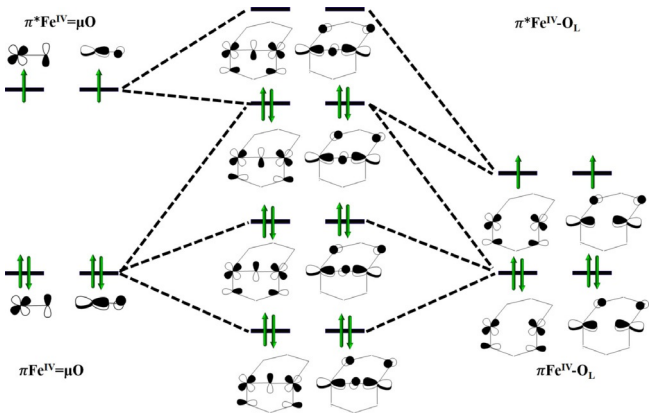

Figure 10. The qualitative MO diagram for the μ-oxo bridged diiron(IV) complex arising from iron(IV)-oxo and iron(IV)carboxamido fragments.

Discussion

Electronic structure of dinuclear iron oxo complexes I–III

In all three complexes **I**–**III**, the ground state is characterized by an antiferromagnetic coupling between the two iron centers. In complex **I**, both Fe^{III} centers possess a high-spin state, leading to the $S=0$ ground state whereas in complex **II**, Fe^{III} possesses a high-spin state whereas Fe^{IV} possesses an intermediate-spin state, leading to $S=3/2$ as the ground state. For complex **III**, both the Fe^{IV} centers possess intermediate spin, leading again to the $S=0$ ground state. The estimate of magnetic coupling, however, was found to vary drastically among the three complexes (−145.4 cm^{-1} for **I**, −335.6 cm^{-1} for **II**, and −114.5 cm^{-1} for **III**) and this is essentially due to the varying nature of the $d_{xz}/d_{yz}|p_x/p_y|d_{xz}/d_{yz}$ overlaps between the two centers. Calculation of the absorption spectra reveals characteristic peaks for each species corresponding to electron transfer from one metal center to the another and this can be used as a guide to detect these species at low temperatures (436, 517 nm for complex **I**, very low energy IVCT type bands for complex **II**, and a peak at 534 nm for complex **III**). For complex **II**, the Fe^{IV}=μO bond lengths are estimated to be 1.704 Å, which is slightly longer than the monomeric $S=1$ and $S=2$ states of Fe^{IV}-oxo, yet catalytic activity has not been witnessed for this species. This is essentially due to strong spin polarization and energetically accessible valance delocalization, leading to a reduction of formal charge on the Fe^{IV} center. Isomer shift values are found to vary from 0.417 to −0.039 mm s^{-1} as we move from the Fe^{III} to Fe^{IV} center. For complex **III**, the Fe^{IV} centers are found to be asymmetric with a longer and a shorter Fe^{IV}-oxo bond (1.825 and 1.741 Å), suggesting a scenario of Fe^{IV}–μO=Fe^{IV} type bonding. A qualitative MO diagram depicting various interactions of the Fe^{IV} centers is shown in Figure 10. On one end, a Fe^{IV}=μO fragment and on the other end a Fe^{IV}(carboxamido)$_2$ fragment are assumed. The two unpaired electrons present on the Fe^{IV} centers pair up in the antibonding orbitals, leading to the $S=0$ ground state. Significant antibonding interactions between the Fe^{IV} center and μ-oxo groups are reduced owing to bonding interactions with the carboxamido moiety in the HOMO. This also places the LUMO close in energy and leads to several low-lying spin states for this species. This in turn helps to generate very high reactivity.

C–H versus O–H bond activation

Dual catalytic abilities are observed for complex **III**, where it is found to activate inert C–H bonds such as those of cyclohexane and also selectively activates the O–H bond of *tert*-butanol. The C–H bond activation proceeds via a $S=4$ state arising from the quintet states of individual Fe^{IV}-oxo center and $S=2$ states arising from the triplet state of individual Fe^{IV}-oxo centers. Although the ground state is characterized by antiferromagnetic coupling, the ferromagnetic state is found to offer greater reactivity.

This is essentially due to the exchange-enhanced reactivity corresponding to the ferromagnetic state.[61] In the dinuclear framework, to maximize the exchange-enhanced reactivity, the catalyst switches the magnetic coupling from antiferromagnetic to ferromagnetic at the transition state. At the ferromagnetic state, the spins on both the centers are of the same type, leading to a large number of unpaired electrons in the ground state and this eases the catalytic transformations.

In addition, the σ* character of the FeO bond rationalizes the electrophilic nature of the active catalyst. A low-lying FeO σ* orbital is found to yield a lower energy barrier, however, the energy also needs to be compared with the HOMO of the donor atoms as it transfers the electron to the FeO σ* orbital. The energy difference between the donor and acceptor gives some ideas for the reactivity and this has been employed previously to rationalize the reactivity of some Fe^{IV}=O species.[26] To understand the role of the FeO σ* orbital in our case, we have also estimated the energy difference between the FeO σ* and HOMO orbital of cyclohexane and this is found to be 2.2 eV in the solution phase. This value is comparable to the values estimated previously for some model complexes, which are predicted to activate inert C–H bonds such as those of methane.[26] In species ^{1}**III**$_{is}$, the FeO σ* orbital is found to be the LUMO and has significant d_{z^2} contributions on both the metal centers, suggesting strong electron delocalization stabilizing this orbital, leading to a relatively small gap between the donor and acceptor and this is translated into smaller barrier heights.

Although the ground state and the low-lying transition states have different multiplicity, the energies correspond to the exchange interaction between the metal centers and this parameter are known to be very sensitive to small structural alterations. Particularly, Fe–O distances and Fe-μO-Fe angles are significantly altered[62] at the transitions state compared with that of the reactant to effect this switch in the nature of magnetic coupling during the course of the reaction. This clearly suggests that exchange coupling plays an important role in controlling the reactivity of this species. In addition, for the C–H bond activation, a novel combination σ_{Fe1}–π_{Fe2} pathway is discovered, revealing the nature of the electronic cooperativity present in this species. Further, an internal electron transfer from one Fe atom to another during the course of the reaction is witnessed. All these effects put together promotes reactivity nearly 1000 times faster than a monomeric Fe^{IV}-oxo complexes where none of them are feasible.

For the O–H bond activation, the reactions are found to occur in the $S=2$ ($S=0$) state, corresponding to the ferromagnetic (antiferromagnetic) coupled state of two $S=1$ state Fe^{IV} centers. Here, the high-spin solution is high lying in energy and the reaction is found to proceed only on the intermediate spin surface of the Fe^{IV} centers. In this case, spin-flip transitions are not involved and the structural change during the course of the reaction is expected to alter the magnetic coupling so as to allow the reaction to proceed in a $S=2$ coupled state. In the C–H bond activation reaction, the newly forming Fe–μO···H_{cyc} are only partially formed at the transition state whereas in the O–H bond activation the newly forming Fe–μO···H–O bond is fully formed and thus corresponds to a complete one-electron transfer from the substrate to the metal centers. The weakly antibonding π* orbitals of the $S=2$ state facilitate this transfer, leading to the observation of a π–π type pathway for this species. Here, also a significant electronic cooperativity between the two metal centers during the course of the reaction is noticeable.

Experimentally, the second-order rate constants are estimated to be 0.081 and 0.30 $M^{-1}s^{-1}$ for the C–H and O–H bonds, respectively, suggesting faster oxidation with the *tert*-butanol than cyclohexane. The computed data is consistent with these observations. The barrier height computed for the C–H bond activation is marginally larger than that of the O–H bond activation (126.4 vs. 118.2 kJ mol^{-1}). In addition, the O–H bond activation is found to occur exclusively on the intermediate spin surface whereas a MECP is required to access the energetically low-lying C–H bond activation transition state. This is likely to add a further energy penalty for the oxidation of cyclohexane. More importantly, our transition state for the O–H activation reveals that both the O–H bond and the C–C bond cleavage are simultaneous, leading to the final product with just one kinetic barrier, whereas the C–H bond activation of cyclohexane requires the abstraction of another H atom from the cyclohexyl radical, leading to the product. Although the second step is unlikely to be rate determining, a kinetic barrier for the abstraction is likely to be present, leading to a slower reaction rate.[14b] Although complex **III** is found to activate the C–H bonds, in the *tert*-butanol substrate, it selectively cleaves the O–H bonds instead of weaker C–H bonds.[14b] This selectivity stems from hydrogen-bonding interactions between the O–H bonds of the *tert*-butanol and the μ-oxo group. This hydrogen-bonding interaction generates a precatalytic species leading to a selective cleavage of the O–H bonds in *tert*-butanol.

Conclusions

The conclusions derived from our work are summarized below.

Our computed results reveal that for all three diiron complexes (**I**–**III**), the ground state is characterized by an antiferromagnetic coupling between the two iron centers regardless of the nature of the oxidation states. The *J* values are estimated to be −145.4, −335.6, and −114.5 cm^{-1} for complexes **I**–**III** and the computed absorption and parameters are in agreement with the experiments.

Our calculations reveal an asymmetric Fe^{IV}-oxo center in complex **III** with a bonding scenario of Fe^{IV}–μO=Fe^{IV}. Although the formal oxidation states are the same, a valance localized picture is visible for this species with the shorter Fe^{IV}–μO center proactively involved in the catalytic reactions. The presence of another Fe^{IV} center and the carboxamido bridges weaken the Fe^{IV}=μO π bonds, leading to relatively longer bond lengths compared with any high-spin/low-spin monomeric Fe^{IV}=O reported.

The C–H bond activation is found to proceed with a barrier height of 126.4 kJ mol^{-1} at the coupled $S=4$ state of the dimer. A switch in the nature of the exchange coupling is witnessed as we proceed from the reactant to the transition state, revealing the importance of the exchange coupling in controlling the reactivity of this species. The significantly exchange-enhanced reactivity of the $S=4$ state leads to faster reactions. In addition, significant electronic cooperativity between the two metal centers is witnessed where an internal electron transfer from one metal to the other during the course of the reaction was observed. This suggests that multiple metal centers are likely to be more reactive as has been witnessed lately for tetranuclear and pentanuclear complexes possessing Fe^{IV}-oxo species.[58–59] The C–H bond activation is found to proceed via a mixed σ–π pathway, combining the advantage of both the σ and the π channels, leading to lower barrier heights. The O–H bond activation is found to occur in the $S=2$ and $S=0$ states, corresponding to the ferro- and antiferromagnetically coupled triplet states of Fe^{IV}-oxo species. Here, the high-spin states are not involved in the reactivity. The barrier height at the $S=2$ state is computed to be 118.2 kJ mol^{-1}, which is lower than that computed for the C–H bond activation step. In addition, the transition state reveals a π–π type pathway. Importantly, this reaction is found to occur in one step where both the O–H and C–C bonds cleave simultaneously, leading to the desired products. One step reaction with a reduction in the barrier height leads to faster reactivity with the *tert*-butanol than cyclohexane.

Spin coupling leads to several close-lying spin states and the possibility of electronic cooperativity leads to the observation of the unusual dual catalytic abilities where the catalyst is found to react via high-spin/intermediate-spin Fe^{IV} centers for

the C–H bond activation whereas only via intermediate-spin Fe^{IV} centers for the O–H bond activation. The catalyst judiciously chooses the desired spin states based on the nature of the substrate and effects the transformations. These findings are expected to have a decisive impact on the dinuclear reactivity reported for metalloenzymes such as sMMO.

To this end, here, we have described in detail the electronic structure and spectral characteristics of oxo-bridged dinuclear iron complexes. We have employed DFT methods to shed light on the dual catalytic abilities (C–H and O–H bond activation). The magnetic coupling and electronic cooperativity between the metal centers are found to play important roles in regulating the very high reactivity. These results will have consequences beyond the examples studied here.

Acknowledgments

G.R. acknowledges financial support from the Government of India through the Department of Science and Technology (Grant EMR/2014/000247) and DST Nanomission for funding and generous computational resources from the Indian Institute of Technology-Bombay. A.A. also would like to acknowledge the financial support from DST-SERB (ECR/2016/001111). A.A. and M.A. thank CSIR/IIT Bombay for a SRF fellowship.

Conflict of interest

The authors declare no conflict of interest.

Keywords: C–H activation · O–H activation · density functional calculations · diiron-oxo species · electronic cooperation

[1] a) T. Punniyamurthy, S. Velusamy, J. Iqbal, *Chem. Rev.* **2005**, *105*, 2329 – 2364; b) W. Nam, *Acc. Chem. Res.* **2007**, *40*, 522 – 531; c) S. Shaik, W. Lai, H. Chen, Y. Wang, *Acc. Chem. Res.* **2010**, *43*, 1154 – 1165; d) E. I. Solomon, U. M. Sundaram, T. E. Machonkin, *Chem. Rev.* **1996**, *96*, 2563 – 2606; e) M. Costas, M. P. Mehn, M. P. Jensen, L. Que, Jr., *Chem. Rev.* **2004**, *104*, 939 – 986.

[2] a) S. J. Lippard, *Philos. Trans. R. Soc. London Ser. A* **2005**, *363*, 861 – 877; b) M. Merkx, D. A. Kopp, H. S. Matthew, J. L. Blazyk, J. Muller, S. J. Lippard, *Angew. Chem. Int. Ed.* **2001**, *40*, 2782 – 2807; *Angew. Chem.* **2001**, *113*, 2860 – 2888; c) A. D. N. Vaz, D. F. Mcginnity, M. J. Coon, *Proc. Natl. Acad. Sci. USA* **1998**, *95*, 3555 – 3560; d) B. E. Eser, E. W. Barr, P. A. Frantorn, L. Saleh, J. M. Bollinger, C. Krebs, P. F. Fitzpatrick, *J. Am. Chem. Soc.* **2007**, *129*, 11334 – 11335; e) C. Krebs, D. G. Fujimori, C. T. Walsh, J. M. Bollinger, *Acc. Chem. Res.* **2007**, *40*, 484 – 492; f) J. M. Bollinger, C. Krebs, *J. Inorg. Biochem.* **2006**, *100*, 586 – 605.

[3] a) I. G. Denisov, T. M. Makris, S. G. Sligar, I. Schlichting, *Chem. Rev.* **2005**, *105*, 2253 – 2278; b) S. Shaik, H. Hirao, D. Kumar, *Acc. Chem. Res.* **2007**, *40*, 532 – 542; c) J. U. Rohde, J. H. In, M. H. Lim, W. W. Brennessel, M. R. Bukowski, A. Stubna, E. Munck, W. Nam, L. Que, Jr., *Science* **2003**, *299*, 1037 – 1039; d) J. England, Y. Guo, E. R. Farquhar, V. G. Young, Jr., E. Munck, L. Que, Jr., *J. Am. Chem. Soc.* **2010**, *132*, 8635 – 8644; e) E. J. Klinker, J. Kaizer, W. W. Brennessel, N. L. Woodrum, C. J. Cramer, L. Que, Jr., *Angew. Chem. Int. Ed.* **2005**, *44*, 3690 – 3694; *Angew. Chem.* **2005**, *117*, 3756 – 3760; f) B. Pandey, A. Ansari, N. Vyas, G. Rajaraman, *J. Chem. Sci.* **2015**, *127*, 343 – 352.

[4] a) O. V. Makhlynets, E. V. Rybak-Akimova, *Chem. Eur. J.* **2010**, *16*, 13995 – 14006; b) O. V. Makhlynets, P. Das, S. Taktak, M. Flook, R. Mas-Balleste, E. V. Rybak-Akimova, L. Que, Jr., *Chem. Eur. J.* **2009**, *15*, 13171 – 13180; c) A. Ansari, G. Rajaraman, *Dataset Papers Sci.* **2014**, 753131; d) S. P. de Visser, J. U. Rohde, Y. M. Lee, J. Cho, W. Nam, *Coord. Chem. Rev.* **2013**, *257*, 381 – 393.

[5] L. Que, Jr., W. B. Tolman, *Nature* **2008**, *455*, 333 – 340.

[6] a) S. Taktak, M. Flook, B. M. Foxman, L. Que, Jr., E. V. Rybak-Akimova, *Chem. Commun.* **2005**, 5301 – 5303; b) P. Comba, G. Rajaraman, *Inorg. Chem.* **2007**, *46*, 3826 – 3838.

[7] a) K. Cho, H. Chen, D. Janardanan, S. P. de Visser, S. Shaik, W. Nam, *Chem. Commun.* **2012**, *48*, 2189 – 2191; b) W. Nam, J. S. Valentine, *New J. Chem.* **1989**, *13*, 677 – 682; c) R. A. Leising, R. E. Norman, L. Que, Jr., *Inorg. Chem.* **1990**, *29*, 2553 – 2555; d) R. H. Fish, M. S. Konings, K. J. Oberhausen, R. H. Fong, W. M. Yu, G. Christou, J. B. Vincent, D. K. Coggin, R. M. Buchanan, *Inorg. Chem.* **1991**, *30*, 3002 – 3006; e) R. A. Leising, J. Kim, M. A. Perez, L. Que, Jr., *J. Am. Chem. Soc.* **1993**, *115*, 9524 – 9530; f) C. Kim, K. Chen, J. Kim, L. Que, Jr., *J. Am. Chem. Soc.* **1997**, *119*, 5964 – 5965; g) S. Mukerjee, A. Stassinopoulos, J. P. Caradonna, *J. Am. Chem. Soc.* **1997**, *119*, 8097 – 8098.

[8] a) M. Sono, M. P. Roach, E. D. Coulter, J. H. Dawson, *Chem. Rev.* **1996**, *96*, 2841 – 2887; b) E. Y. Tshuva, S. J. Lippard, *Chem. Rev.* **2004**, *104*, 987 – 1011; c) S. Hong, Y.-M. Lee, W. Shin, S. Fukuzumi, W. Nam, *J. Am. Chem. Soc.* **2009**, *131*, 13910 – 13911; d) J. Yoon, S. A. Wilson, Y. K. Jang, M. S. Seo, K. Nehru, B. Hedman, K. O. Hodgson, E. Bill, E. I. Solomon, W. Nam, *Angew. Chem. Int. Ed.* **2009**, *48*, 1257 – 1260; *Angew. Chem.* **2009**, *121*, 1283 – 1286; e) Y.-M. Lee, S. Hong, Y. Morimoto, W. Shin, S. Fukuzumi, W. Nam, *J. Am. Chem. Soc.* **2010**, *132*, 10668 – 10670; f) M. Ansari, N. Vyas, A. Ansari, G. Rajaraman, *Dalton Trans.* **2015**, *44*, 15232 – 15243.

[9] a) B. Behrouzian, P. H. Buist, *Curr. Opin. Chem. Biol.* **2002**, *6*, 577 – 582; b) W. Nam, *Acc. Chem. Res.* **2007**, *40*, 465 – 465; c) P. E. M. Siegbahn, T. Borowski, *Acc. Chem. Res.* **2006**, *39*, 729 – 738; d) M. H. Baik, M. Newcomb, R. A. Friesner, S. J. Lippard, *Chem. Rev.* **2003**, *103*, 2385 – 2419; e) S. Shaik, D. Kumar, S. P. de Visser, A. Altun, W. Thiel, *Chem. Rev.* **2005**, *105*, 2279 – 2328.

[10] a) G. C. Dismukes, *Chem. Rev.* **1996**, *96*, 2909 – 2926; b) C. A. Ramsden, P. A. Riley, *Bioorg. Med. Chem.* **2014**, *22*, 2388 – 2395; c) P. Jayapal, A. Ansari, G. Rajaraman, *Inorg. Chem.* **2015**, *54*, 11077 – 11082; d) P. Jayapal, G. Rajaraman, *Phys. Chem. Chem. Phys.* **2012**, *14*, 9050 – 9053; e) S. F. Ye, G. Q. Xue, I. Krivokapic, T. Petrenko, E. Bill, L. Que, Jr., F. Neese, *Chem. Sci.* **2015**, *6*, 2909 – 2921; f) L. H. Do, G. Q. Xue, L. Que Jr., S. J. Lippard, *Inorg. Chem.* **2012**, *51*, 2393 – 2402.

[11] M. A. Cranswick, K. K. Meier, X. P. Shan, A. Stubna, J. Kaizer, M. P. Mehn, E. Munck, L. Que, Jr., *Inorg. Chem.* **2012**, *51*, 10417 – 10426.

[12] R. S. Hanson, T. E. Hanson, *Microbiol. Rev.* **1996**, *60*, 439 – 471.

[13] H. H. T. Nguyen, S. J. Elliott, J. H. K. Yip, S. I. Chan, *J. Biol. Chem.* **1998**, *273*, 7957 – 7966.

[14] a) A. Ghosh, F. T. de Oliveira, T. Yano, T. Nishioka, E. S. Beach, I. Kinoshita, E. Munck, A. D. Ryabov, C. P. Horwitz, T. J. Collins, *J. Am. Chem. Soc.* **2005**, *127*, 2505 – 2513; b) D. Wang, E. R. Farquhar, A. Stubna, E. Munck, L. Que, *Nat. Chem.* **2009**, *1*, 145 – 150; c) S. A. Stoian, G. Q. Xue, E. L. Bominaar, L. Que, Jr., E. Munck, *J. Am. Chem. Soc.* **2014**, *136*, 1545 – 1558.

[15] a) G. Q. Xue, A. Pokutsa, L. Que, Jr., *J. Am. Chem. Soc.* **2011**, *133*, 16657 – 16667; b) G. Xue, D. Wang, R. De Hont, A. T. Fiedler, X. Shan, E. Münck, L. Que, *Proc. Natl. Acad. Sci. USA* **2007**, *104*, 20713 – 20718; c) J. R. Frisch, R. McDonnell, E. V. Rybak-Akimova, L. Que, Jr., *Inorg. Chem.* **2013**, *52*, 2627 – 2636; d) D. Wang, L. Que, *Chem. Commun.* **2013**, *49*, 10682 – 10684; e) L. Bernasconi, P. Belanzoni, E. J. Baerends, *Phys. Chem. Chem. Phys.* **2011**, *13*, 15272 – 15282; f) M. P. Hendrich, E. Munck, B. G. Fox, J. D. Lipscomb, *J. Am. Chem. Soc.* **1990**, *112*, 5861 – 5865.

[16] L. D. Slep, A. Mijovilovich, W. Meyer-Klaucke, T. Weyhermuller, E. Bill, E. Bothe, F. Neese, K. Wieghardt, *J. Am. Chem. Soc.* **2003**, *125*, 15554 – 15570.

[17] a) H. Basch, K. Mogi, D. G. Musaev, K. Morokuma, *J. Am. Chem. Soc.* **1999**, *121*, 7249 – 7256; b) P. E. M. Siegbahn, R. H. Crabtree, *J. Am. Chem. Soc.* **1997**, *119*, 3103 – 3113; c) G. Q. Xue, C. Y. Geng, S. F. Ye, A. T. Fiedler, F. Neese, L. Que, Jr., *Inorg. Chem.* **2013**, *52*, 3976 – 3984; d) K. Yoshizawa, *Acc. Chem. Res.* **2006**, *39*, 375 – 382; e) M. Torrent, D. G. Musaev, K. Morokuma, *J. Phys. Chem. B* **2001**, *105*, 322 – 327; f) M. Torrent, K. Mogi, H. Basch, D. G. Musaev, K. Morokuma, *J. Phys. Chem. B* **2001**, *105*, 8616 – 8628; g) D. Lee, B. Pierce, C. Krebs, M. P. Hendrich, B. H. Huynh, S. J. Lippard, *J. Am. Chem. Soc.* **2002**, *124*, 3993 – 4007; h) W.-G. Han, T. Lovell, T. Liu, L. Noodleman, *Inorg. Chem.* **2003**, *42*, 2751 – 2758; i) K. Yoshizawa, T. Ohta, T. Yamabe, R. Hoffmann, *J. Am. Chem. Soc.* **1997**, *119*, 12311 –

12321; j) S. V. Kryatov, E. V. Rybak-Akimova, S. Schindler, *Chem. Rev.* **2005**, *105*, 2175 – 2226; k) P. E. Siegbahn, *Inorg. Chem.* **1999**, *38*, 2880 – 2889.

[18] M. G. Quesne, D. Senthilnathan, D. Singh, D. Kumar, P. Maldivi, A. B. Sorokin, S. P. De Visser, *ACS Catal.* **2016**, *6*, 2230 – 2243.

[19] a) S.-P. Huang, Y. Shiota, K. Yoshizawa, *Dalton Trans.* **2013**, *42*, 1011 – 1023; b) T. Saito, Y. Kataoka, Y. Nakanishi, Y. Kitagawa, T. Kawakami, S. Yamanaka, M. Okumura, K. Yamaguchi, *Supramol. Chem.* **2011**, *23*, 83 – 87.

[20] Gaussian 09, Revision 02, M. J. Frisch, G. W. Trucks, H. B. Schlegel, G. E. Scuseria, M. A. Robb, J. R. Cheeseman, G. Scalmani, V. Barone, B. Mennucci, G. A. Petersson, H. Nakatsuji, M. Caricato, X. Li, H. P. Hratchian, A. F. Izmaylov, J. Bloino, G. Zheng, J. L. Sonnenberg, M. Hada, M. Ehara, K. Toyota, R. Fukuda, J. Hasegawa, M. Ishida, T. Nakajima, Y. Honda, O. Kitao, H. Nakai, T. Vreven, J. A. Montgomery, Jr., J. E. Peralta, F. Ogliaro, M. Bearpark, J. J. Heyd, E. Brothers, K. N. Kudin, V. N. Staroverov, R. Kobayashi, J. Normand, K. Raghavachari, A. Rendell, J. C. Burant, S. S. Iyengar, J. Tomasi, M. Cossi, N. Rega, J. M. Millam, M. Klene, J. E. Knox, J. B. Cross, V. Bakken, C. Adamo, J. Jaramillo, R. Gomperts, R. E. Stratmann, O. Yazyev, A. J. Austin, R. Cammi, C. Pomelli, J. W. Ochterski, R. L. Martin, K. Morokuma, V. G. Zakrzewski, G. A. Voth, P. Salvador, J. J. Dannenberg, S. Dapprich, A. D. Daniels, Ö. Farkas, J. B. Foresman, J. V. Ortiz, J. Cioslowski, D. J. Fox, Gaussian, Inc. Wallingford, CT, **2009**.

[21] A. Ansari, A. Kaushik, G. Rajaraman, *J. Am. Chem. Soc.* **2013**, *135*, 4235 – 4249.

[22] a) M. Güell, J. M. Luis, M. Sola, M. Swart, *J. Phys. Chem. A* **2008**, *112*, 6384 – 6391; b) S. Grimme, J. Antony, S. Ehrlich, H. Krieg, *J. Chem. Phys.* **2010**, *132*, 154104.

[23] a) T. H. Dunning, Jr., P. J. Hay, in *Modern Theoretical Chemistry, Vol. 3* (Ed.: H. F. Schaefer), Plenum, New York, **1976**; b) P. J. Hay, W. R. Wadt, *J. Chem. Phys.* **1985**, *82*, 270 – 283; c) P. J. Hay, W. R. Wadt, *J. Chem. Phys.* **1985**, *82*, 299 – 310; d) W. R. Wadt, P. J. Hay, *J. Chem. Phys.* **1985**, *82*, 284 – 298.

[24] R. Ditchfield, W. J. Hehre, J. A. Pople, *J. Chem. Phys.* **1971**, *54*, 724 – 728.

[25] F. Weigend, R. Ahlrichs, *Phys. Chem. Chem. Phys.* **2005**, *7*, 3297 – 3305.

[26] L. Bernasconi, E. J. Baerends, *J. Am. Chem. Soc.* **2013**, *135*, 8857 – 8867.

[27] F. G. Cantú Reinhard, A. S. Faponle, S. P. de Visser, *J. Phys. Chem. A* **2016**, *120*, 9805 – 9814.

[28] B. Pandey, M. Jaccob, G. Rajaraman, *Chem. Commun.* **2017**, *53*, 3193 – 3196.

[29] G. A. Zhurko, ChemCraft software, version 1.6, **2014**.

[30] a) P. Fluckiger, H. P. Luthi, S. Portmann, J. Weber, *Molekel 4.3*, Swiss Center for Scientific Computing, Manno, Switzerland, **2000**; b) S. Portmann, H. P. Luthi, *Chimia* **2000**, *54*, 766 – 770.

[31] a) L. Noodleman, *J. Chem. Phys.* **1981**, *74*, 5737 – 5743; b) L. Noodleman, E. R. Davidson, *Chem. Phys.* **1986**, *109*, 131 – 143.

[32] F. Neese, *WIRES: Comp. Mol. Sci.* **2012**, *2*, 73 – 78.

[33] a) E. van Lenthe, E. J. Baerends, J. G. Snijders, *J. Chem. Phys.* **1993**, *99*, 4597 – 4610; b) E. van Lenthe, E. J. Baerends, J. G. Snijders, *J. Chem. Phys.* **1994**, *101*, 9783 – 9792.

[34] M. Römelt, S. F. Ye, F. Neese, *Inorg. Chem.* **2009**, *48*, 784 – 785.

[35] A. E. Reed, L. A. Curtiss, F. Weinhold, *Chem. Rev.* **1988**, *88*, 899 – 926.

[36] a) E. Ruiz, S. Alvarez, A. Rodriguez-Fortea, P. Alemany, Y. Pouillon, C. Massobiro, in *Magnetism: Molecules to Materials, Vol. II* (Ed.: J. S. Miller, M. Drillon), Wiley-VCH, Weinheim, **2001**; b) T. Gupta, T. Rajeshkumar, G. Rajaraman, *Phys. Chem. Chem. Phys.* **2014**, *16*, 14568 – 14577; c) S. K. Singh, K. S. Pedersen, M. Sigrist, C. A. Thuesen, M. Schau-Magnussen, H. Mutka, S. Piligkos, H. Weihe, G. Rajaraman, J. Bendix, *Chem. Commun.* **2013**, *49*, 5583 – 5585.

[37] Z. D. Chen, Z. T. Xu, L. Zhang, F. Yan, Z. Y. Lin, *J. Phys. Chem. A* **2001**, *105*, 9710 – 9716.

[38] S. Hazra, S. Bhattacharya, M. K. Singh, L. Carrella, E. Rentschler, T. Weyhermueller, G. Rajaraman, S. Mohanta, *Inorg. Chem.* **2013**, *52*, 12881 – 12892.

[39] Our calculation does not reproduce a very weak feature observed experimentally at 680 nm.

[40] S. S. Leang, F. Zahariev, M. S. Gordon, *J. Chem. Phys.* **2012**, *136*, 104101.

[41] S. F. Ye, C. Y. Geng, S. Shaik, F. Neese, *Phys. Chem. Chem. Phys.* **2013**, *15*, 8017 – 8030.

[42] R. F. De Hont, G. Q. Xue, M. P. Hendrich, L. Que, Jr., E. L. Bominaar, E. Munck, *Inorg. Chem.* **2010**, *49*, 8310 – 8322.

[43] F. Weinhold, C. R. Landis, *Valency and Bonding: A Natural Bond Orbital Donor-Acceptor Perspective*, Cambridge University Press, Cambridge, **2005**.

[44] S. Ghosh, S. K. Singh, S. Tewary, G. Rajaraman, *Dalton Trans.* **2013**, *42*, 16490 – 16493.

[45] L. M. Dassama, A. Silakov, C. M. Krest, J. C. Calixto, C. Krebs, J. M. Bollinger, Jr., M. T. Green, *J. Am. Chem. Soc.* **2013**, *135*, 16758 – 16761.

[46] B. J. Brazeau, R. N. Austin, C. Tarr, J. T. Groves, J. D. Lipscomb, *J. Am. Chem. Soc.* **2001**, *123*, 11831 – 11837.

[47] a) J. Kaizer, E. J. Klinker, N. Y. Oh, J. U. Rohde, W. J. Song, A. Stubna, J. Kim, E. Munck, W. Nam, L. Que, Jr., *J. Am. Chem. Soc.* **2004**, *126*, 472 – 473; b) D. P. Galonic, E. W. Barr, C. T. Walsh, J. M. Bollinger, Jr., C. Krebs, *Nat. Chem. Biol.* **2007**, *3*, 113 – 116.

[48] E. V. Kudrik, P. Afanasiev, L. X. Alvarez, P. Dubourdeaux, M. Clémancey, J.-M. Latour, G. Blondin, D. Bouchu, F. Albrieux, S. E. Nefedov, *Nat. Chem.* **2012**, *4*, 1024 – 1029.

[49] a) D. Wang, K. Ray, M. J. Collins, E. R. Farquhar, J. R. Frisch, L. Gomez, T. A. Jackson, M. Kerscher, A. Waleska, P. Comba, M. Costas, L. Que, Jr., *Chem. Sci.* **2013**, *4*, 282 – 291; b) B. Meunier, S. P. de Visser, S. Shaik, *Chem. Rev.* **2004**, *104*, 3947 – 3980.

[50] J. C. Schöneboom, S. Cohen, H. Lin, S. Shaik, W. Thiel, *J. Am. Chem. Soc.* **2004**, *126*, 4017 – 4034.

[51] a) T. Kamachi, T. Kouno, W. Nam, K. Yoshizawa, *J. Inorg. Biochem.* **2006**, *100*, 751 – 754; b) J. T. Groves, T. E. Nemo, *J. Am. Chem. Soc.* **1983**, *105*, 6243 – 6248.

[52] A. Ansari, P. Jayapal, G. Rajaraman, *Angew. Chem. Int. Ed.* **2015**, *54*, 564 – 568; *Angew. Chem.* **2015**, *127*, 574 – 578.

[53] D. Schröder, S. Shaik, H. Schwarz, *Acc. Chem. Res.* **2000**, *33*, 139 – 145.

[54] J. N. Harvey, M. Aschi, H. Schwarz, W. Koch, *Theor. Chem. Acc.* **1998**, *99*, 95 – 99.

[55] a) M. Y. Pau, J. D. Lipscomb, E. I. Solomon, *Proc. Natl. Acad. Sci. USA* **2007**, *104*, 18355 – 18362; b) D. Danovich, S. Shaik, *J. Am. Chem. Soc.* **1997**, *119*, 1773 – 1786.

[56] a) P. Barman, A. K. Vardhaman, B. Martin, S. J. Wörner, C. V. Sastri, P. Comba, *Angew. Chem. Int. Ed.* **2015**, *54*, 2095 – 2099; *Angew. Chem.* **2015**, *127*, 2123 – 2127; b) S. Ye, F. Neese, *Proc. Natl. Acad. Sci. USA* **2011**, *108*, 1228 – 1233; c) H. Tang, J. Guan, H. Liu, X. Huang, *Dalton Trans.* **2013**, *42*, 10260 – 10270.

[57] a) M. Jaccob, A. Ansari, B. Pandey, G. Rajaraman, *Dalton Trans.* **2013**, *42*, 16518 – 16526; b) D. Usharani, D. C. Lacy, A. Borovik, S. Shaik, *J. Am. Chem. Soc.* **2013**, *135*, 17090 – 17104.

[58] O. Masaya, K. Mio, K. Reiko, K. Yuki, Y. Takeshi, H. Shinya, K. K. P. Vijayendran, Y. Masaki, Y. Ko, K. Satoshi, M. Shigeyuki, *Nature* **2016**, *530*, 465 – 468.

[59] G. de Ruiter, N. B. Thompson, M. K. Takase, T. Agapie, *J. Am. Chem. Soc.* **2016**, *138*, 1486 – 1489.

[60] D. Griller, K. U. Ingold, *Acc. Chem. Res.* **1980**, *13*, 317 – 323.

[61] S. Shaik, H. Chen, D. Janardanan, *Nat. Chem.* **2012**, *4*, 19 – 27.

[62] L. Fohlmeister, K. R. Vignesh, F. Winter, B. Moubaraki, G. Rajaraman, R. Pottgen, K. S. Murray, C. Jones, *Dalton Trans.* **2015**, *44*, 1700 – 1708.

Manuscript received: March 8, 2017
Accepted manuscript online: May 12, 2017
Version of record online: July 5, 2017